APL Materials

REVIEW ARTICLE | OCTOBER 20 2023

Towards ultrathin metal-organic frameworks membranes for high-performance separation

Qi Liu ; Heng-Yu Chi ; Shuqing Song ; Ranadip Goswami ; Kumar Varoon Agrawal

APL Mater. 11, 100602 (2023)
https://doi.org/10.1063/5.0169507

Towards ultrathin metal-organic frameworks membranes for high-performance separation

Cite as: APL Mater. 11, 100602 (2023); doi: 10.1063/5.0169507
Submitted: 26 July 2023 • Accepted: 26 September 2023 •
Published Online: 20 October 2023

Qi Liu,[1,2] Heng-Yu Chi,[1] Shuqing Song,[1] Ranadip Goswami,[1] and Kumar Varoon Agrawal[1,a)]

AFFILIATIONS

[1] Laboratory of Advanced Separations, École Polytechnique Fédérale de Lausanne (EPFL), 1950 Sion, Switzerland
[2] College of Chemistry, Chemical Engineering and Materials Science, Soochow University, Suzhou 215123, China

[a)] **Author to whom correspondence should be addressed:** kumar.agrawal@epfl.ch

ABSTRACT

Research on metal-organic frameworks (MOFs) based membranes has gained a lot of attention in the last decade thanks to the unique and highly versatile chemistry of MOFs, which allows one to synthesize a variety of structural dimensions, topologies, pore sizes, pore shapes, functional groups, and chemical environments. For membrane application, the field is rapidly progressing, with the focus shifting from the synthesis of pinhole-free polycrystalline films to the synthesis of ultrathin MOF films on scalable support to surpass the performance of polymeric membranes. In this research update, we review promising methodologies for the synthesis of ultrathin MOF membranes. We then discuss the application of these ultrathin MOF films in gas separation, ion transport and ion–ion separation, and desalination. We then provide our perspective on opportunities and challenges for the future development of ultrathin MOF membranes.

I. INTRODUCTION

Metal-organic frameworks (MOFs) represent an attractive class of materials with exceptionally high porosity where pores can be designed to be in the ultramicropore to mesopore regime.[1–6] MOFs are composed of metal or metal oxide nodes, which are coordinated with organic linkers. Traditionally, MOFs have an ordered framework, although recently, amorphous MOFs have been reported.[7,8] Their topology and chemical composition are uniquely tunable either by pre-synthetic structural design,[1] thanks to the ease of manipulating coordination chemistry, or by postsynthetic modification.[9] This has resulted in a variety of structural dimensions, topologies, pore sizes, pore shapes, functional groups, and chemical environments. This has allowed one to tailor the guest-host interactions, e.g., selective molecular binding and gas diffusivity. These aspects make MOF highly attractive as the selective layer in membrane-based molecular separation, especially when compared to membranes based on other microporous materials such as zeolite (Scheme 1). Motivated by this, there has been extensive research on the synthesis of MOF as a thin polycrystalline film.

Other promising materials for membrane-based separation include polymers,[10–14] carbon molecular sieves (CMS),[15,16] dense metals (Pd for H_2 separation),[17,18] covalent organic frameworks (COFs),[19–21] g-C_3N_4,[22–25] and graphene derivatives.[26–28] Polymeric membranes have been commercialized for gas separation owing to their ease of processing and low raw-material costs. However, their performance is limited by an intrinsic permeability-selectivity trade-off known as the Robeson upper bound.[10–12] Pd membranes have shown one of the best performances for hydrogen purification but suffer from high Capital Expenditure (CAPEX) and stability issues in the presence of CO and H_2S. Nanoporous membranes based on MOFs, zeolite, CMS, and graphene derivatives display improved performance because of highly selective and rapid diffusion through the nanopores; however, a combination of issues such as high synthetic complexity and reproducibility have been a key bottleneck. Among these, MOF membranes are highly attractive, as explained earlier. Therefore, in its current state, the field of MOF membrane stands to benefit from scalable synthesis protocols resulting in robust selective layers yielding high-performance separation. These three aspects, namely, scalability, a robust selective layer, and high-performance, are discussed below.

Scalable synthetic protocols refer to the ease of fabrication of membranes. Protocols that can be adapted to continuous manufacturing are preferred. In this context, membranes based on a

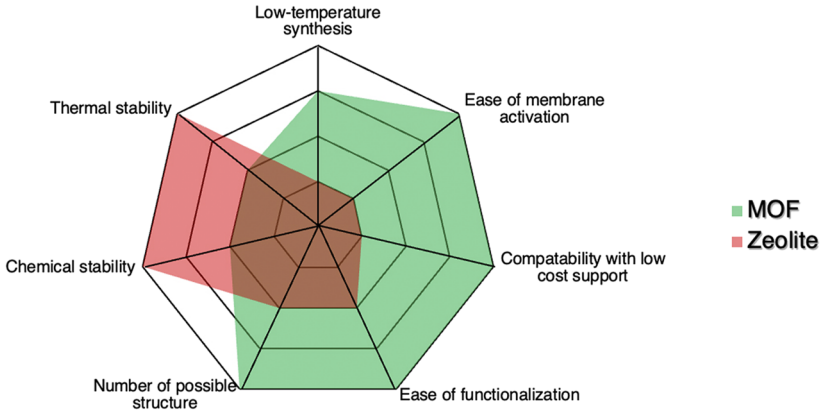

SCHEME 1. A comparison between MOFs and zeolite membranes, which shows as to why MOFs are highly attractive for membrane separation applications.

polymeric selective layer[29–36] have an intrinsic advantage because polymer films can be conveniently deposited as a thin film in a solution. MOF films are not too far from continuous manufacturing. The synthesis of MOF has evolved tremendously from protocols mimicking zeolite film synthesis (i.e., seeded secondary growth). In the last decade, the field has seen accelerated progress in the development of protocols that cut down the time for the synthesis of MOF films to a few minutes at room temperature and can be adapted for continuous manufacturing. Examples include interfacial synthesis, current-driven synthesis, precursor flow mediated synthesis, and filtration. While these methods involve a higher level of complexity compared to simple deposition-based protocols for polymeric membranes, they are amenable to continuous manufacturing upon further development. Furthermore, the highly robust nature of MOF, combined with high-performance separation from MOF membranes, justifies their development as the next-generation platform material for membranes.

Robustness relates to the structural stability of the selective layer in the relevant separation environment. In this respect, MOFs show a distinct advantage compared to polymeric materials. Polymeric films have intrinsic limitations due to the thermodynamically driven aging of the free volume element. Another issue is the swelling of a free volume element in the presence of a solvent or a highly condensable solute, e.g., plasticization with CO_2. These issues lead to loss of permeance (aging-driven) or selectivity (swelling-driven). Thanks to the rigid nature of the coordination bond and the permanent porosity of MOFs, they are not susceptible to aging and swelling. This makes MOF film attractive as a selective layer in several separation applications involving gases, liquids, and ions.[3,37–43] In addition, they provide several distinct advantages. Several MOFs (UiO-66,[44] MIL-101,[45] and MOF-808[46]) show structural integrity at or above 200 °C.[1,47] Several MOFs also show stability in harsh chemical environments. MOF structures composed of high valence metals like Zr[44,47] and Al^{3+}[48] can tolerate acidic and basic solutions to a certain extent including involving those harsh temperatures and chemical conditions. This includes H_2/CO_2 separation (precombustion carbon capture), the pulp and paper industry dealing with black liquor recovery, the chemical and petrochemical industry dealing with acidic or basic streams, etc. This gives MOF membranes an ideal playing field where polymeric membranes are not suitable and more robust materials (e.g., zeolites[48–51]) are relatively challenging to synthesize using scalable protocols.

High-performance relates to either high permeability, high selectivity, or a combination of both. MOFs possess a low-density framework, affording them a high specific surface area. MOFs also yield high diffusivity thanks to their porous topology and high porosity. One can obtain selectivity based on size-sieving (relying on the size exclusion of larger species from MOF pores), kinetic separation (relying on the relative difference in diffusivities), and/or the relative difference in adsorption affinity (relying on the binding of the solute). Yet, to achieve extremely high permeance, one needs to synthesize pinhole-free films that have a thickness below 500 nm. Realizing films with low thickness is highly desired to achieve large permeance, as demonstrated by recent studies.[52–60] This is because permeance is inversely proportional to its thickness. In this regard, scalable protocols yielding ultrathin and pinhole-free MOF film based selective layers are highly attractive. A series of syntheses and strategies have been introduced to fabricate ultrathin MOF membranes, including direct synthesis,[61] secondary growth,[62] electrochemical deposition,[56,60,63–67] vapor deposition,[58,68] interfacial synthesis,[69–73] layer-by-layer (LBL) deposition,[74] nanosheet stacking,[57,59,75–78] postsynthetic modification,[79] etc. Continuous MOF membranes with a selective layer thickness below 50 nm have been successfully prepared.[55] Given the growing importance of this field, we review the reported synthetic protocols to form ultrathin MOF membranes and their reported applications. Finally, we provide a perspective on the challenges and opportunities for ultrathin MOF membranes.

II. SYNTHESIS OF ULTRATHIN MOF MEMBRANES

In order to synthesize ultrathin (<500 nm) MOF membranes, a fine control of the synthesis conditions is necessary, including reactant concentrations, temperature, substrates, etc.[38,77,78,80,81] Several methodologies have been proposed and successfully applied in the fabrication of ultrathin MOF membranes (Scheme 2 and 3). These are direct synthesis,[61] secondary growth,[62] electrochemical deposition,[56,60,63–67] vapor deposition,[58,68] interfacial synthesis,[69–73]

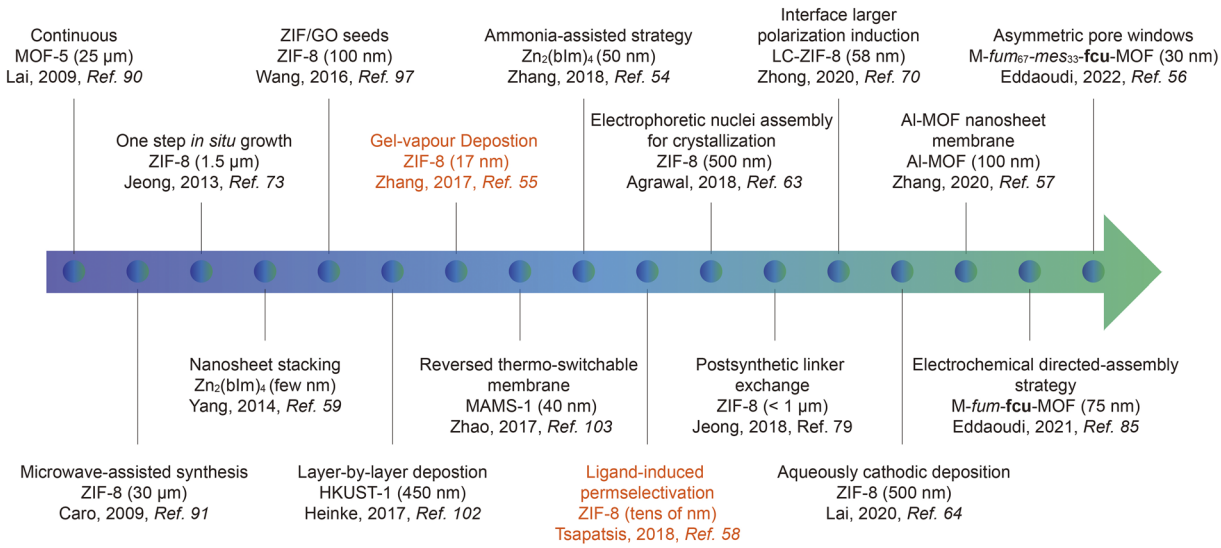

SCHEME 2. Timeline of syntheses of ultrathin MOF membranes by different strategies, where black and orange colors represent solvent-based or vapor-based synthesis, respectively.

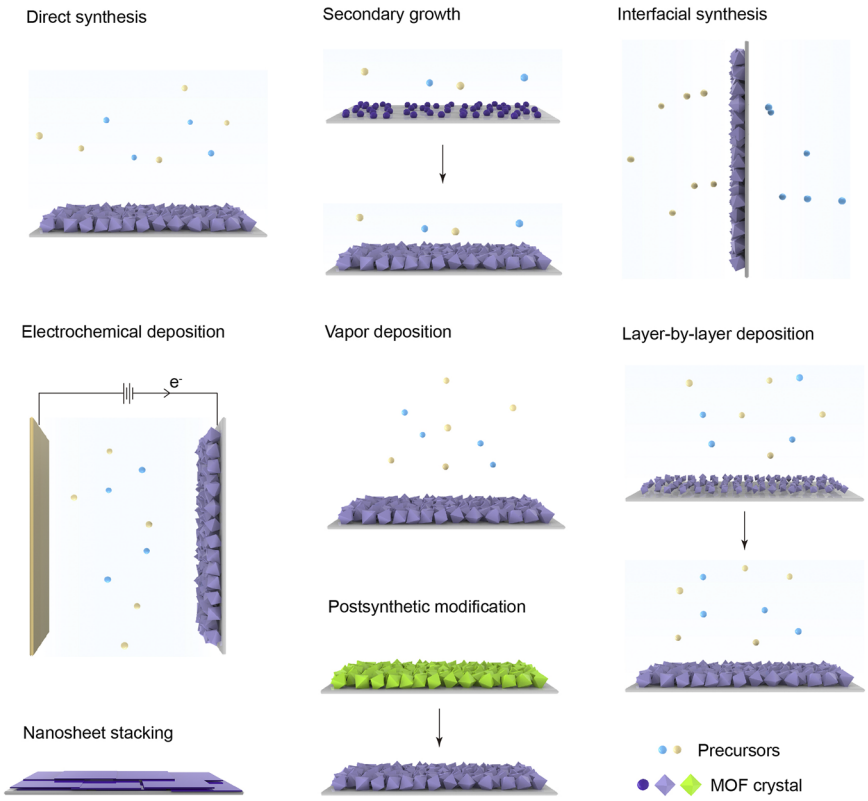

SCHEME 3. Schematic of the syntheses of ultrathin MOF membranes by different strategies.

layer-by-layer deposition,[74] nanosheet stacking,[57,59,75–78] postsynthetic modification,[79] etc., where some are solvent-based and others are vapor-based. The thicknesses of these MOF membranes range from as thin as 17 nm to a few hundred nanometers. Considering that the MOF unit-cell parameters are in the nanometer range, some of the ultrathin MOF membranes contain only tens of unit cells.

Many kinds of MOFs with distinct two-dimensional (2D) and three-dimensional (3D) structures have been utilized to form films, such as ZIF-8,[65,82–83] Zn (bIm)$_4$,[84] Y-fum-**fcu**-MOF,[85] Zr-fum-**fcu**-MOF,[85] HKUST-1,[86] $Zn_2(bim)_3$,[87] NH_2-MIL-53(Al),[76] NH_2-CAU-10(Al),[76] Ica-CD-ZIF-8,[79] etc., indicating the universality of these methods. The structures of MOFs discussed in the research update are summarized in Fig. 1. This is helped by a number of available characterization techniques, which greatly help in understanding the morphology, chemical composition, defects, and structure of the resulting films. For example, optical microscopy along with scanning electron microscopy (SEM) can help understand the morphology. Several linkers are fluorescent, and fluorescent confocal optical microscopy can be used to understand grain-boundary defects along the thickness of MOF. For crystal structure determination, x-ray diffraction (XRD) is an extremely useful way to determine the structure of MOF. For ultrathin oriented films, grazing incidence diffraction has been successfully used to detect lattice planes at an angle to the substrate. The recent emergence of low-dose electron microscopy, helped by the emergence of electron-counting cameras, has allowed the use of transmission electron microscopy (TEM) to characterize beam sensitive MOFs. This, coupled with selected area electron diffraction (SAED), has also been used to

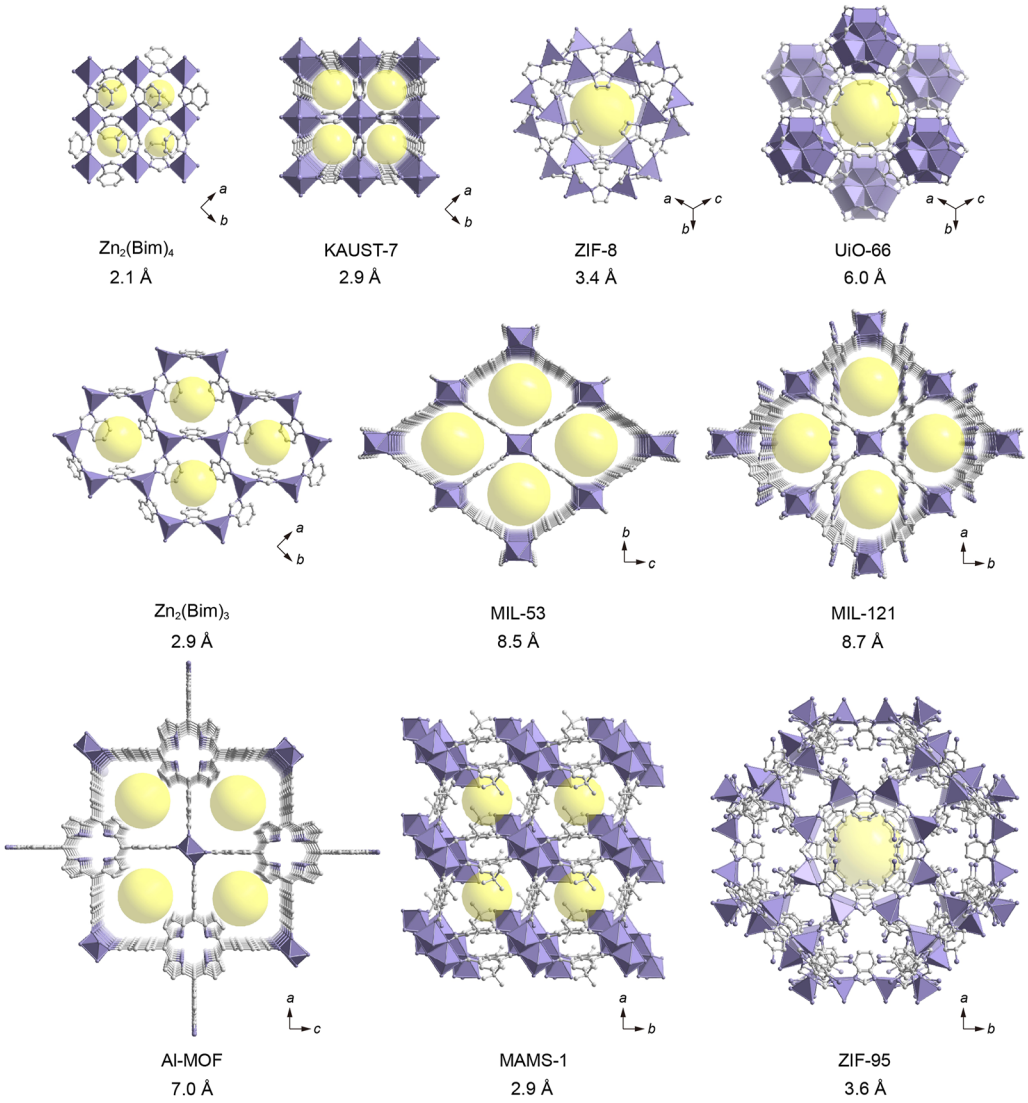

FIG. 1. Representative MOF structures in MOF membranes with their pore aperture sizes.

determine the crystal structure of the film, including the structure of the grain boundary.[88] The growth of extremely thin MOF films or 2D MOFs (e.g., MOF nanosheets) can be characterized by atomic force microscopy (AFM), which can resolve thickness with an accuracy of an angstrom. Finally, the chemical environment and bonding configuration in MOFs can be studied by x-ray photoelectron spectroscopy (XPS), x-ray absorption spectroscopy (XAS), and infrared (IR) spectroscopy. Diffused reflectance infrared Fourier transform spectroscopy (DRIFTS) is quite powerful in identifying open metal site or linker vacancy defects, which in the past has been able to attribute lattice strain and framework flexibility, parameters that greatly influence molecular transport.

Optimization of synthesis conditions with the aid of these diverse characterization techniques allows one to develop a protocol for ultrathin MOF film while solving the constraint of keeping the film continuous and pinhole-free. The description of various synthetic strategies is discussed in detail in the following sections.

A. Direct synthesis

Direct solvothermal synthesis is the common approach for the crystallization of MOFs powder. As a result, it became quite popular for the synthesis of MOF membranes. However, in order to synthesize ultrathin films, fine-tuning and the design of reaction conditions are necessary.[89] In this regard, in 2009, Lai *et al.* reported that MOF-5 membrane was synthesized by immersing porous α-alumina substrate in the reaction solution, and its thickness was 25 μm.[90] In the same year, Caro *et al.* synthesized a 30-μm-thick ZIF-8 membrane on a porous titania support.[91] Although there are a variety of reports about the direct synthesis of MOF membranes, most of them are thick.[92–95] This may come from the uniform heterogeneous nucleation and growth during the synthesis, which calls for thick film to fix this problem. As a result, sophisticated designs were created to make ultrathin MOF films. Zhang *et al.* proposed an ammonia assistance method to synthesize highly oriented $Zn_2(bIm)_4$ (bIm = benzimidazole) membranes by the localized self-conversion of a pre-deposited thin layer of ZnO [Fig. 2(a)].[54] At the beginning, they investigated the formation of a $Zn_2(bIm)_4$ nanosheet from ZnO nanoparticles. These ZnO nanoparticles were prepared by the reaction of $Zn(Ac)_2$ with monoethanolamine (MEA), followed by calcination at 400 °C for 2 h [Fig. 2(b)]. Following this, they reacted with bIm/NH_4OH in a methanol/toluene solution for 3 h. The resultant sample showed a continuous layer was formed on the surface of ZnO nanoparticles [Fig. 2(c)] and expanded with a longer reaction time, accompanied by the disappearance of ZnO nanoparticles [Fig. 2(d)]. This indicates that MOF nanosheets were generated by the localized self-conversion of the ZnO nanoparticles. SAED and XRD data confirmed the crystal structure of $Zn_2(bIm)_4$

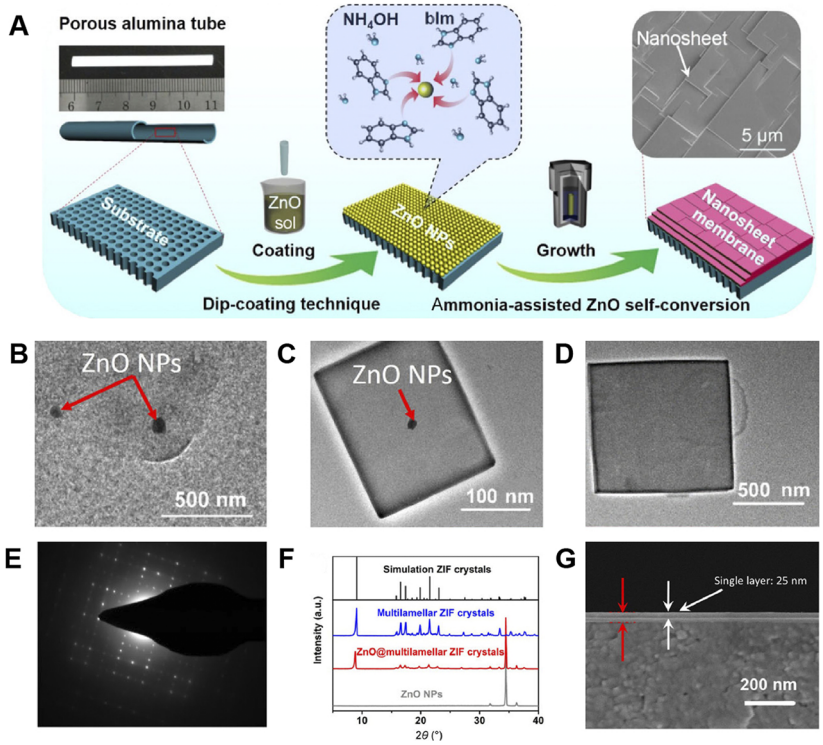

FIG. 2. Synthesis of highly oriented 2D ZIF nanosheet membranes through the solvothermal method. (a) Schematic of the synthesis process. (b)–(d) TEM images of ZnO nanoparticles, partially and fully conversion of ZIF formed from ZnO nanoparticles, respectively. (e) SAED pattern of 2D ZIF nanosheet. (f) XRD pattern of ZnO nanoparticle and 2D ZIF nanosheet. (g) Cross-sectional SEM image of the ultrathin ZIF membrane.[54] Reprinted with permission from Li *et al.*, Nano Res. **11**(4), 1850–1860 (2018). Copyright 2018 Springer Nature.

nanosheets [Figs. 2(e) and 2(f)]. With this result, Zhang *et al.* synthesized a $Zn_2(bIm)_4$ membrane based on the same condition by dip-coating ZnO nanoparticles on a porous alumina tube, and the thickness was only 50 nm [Fig. 2(g)]. It is worth noting that NH_4OH played an important role in determining the oriented morphology of the membrane, where aggregated ZIF particles were formed when NH_4OH was absent.

B. Seeded secondary growth

Seeded secondary growth for MOF film was adopted from extensive research in the field of zeolite membranes in the early days of MOF membrane research.[96] Compared to direct solvothermal synthesis, it has the advantage that the pre-deposited seeds promote heterogeneous nucleation for the formation of a continuous film. In this way, secondary growth reduces defects and pinholes when the target is to make ultrathin film.[62]

In 2016, Wang *et al.* reported an ultrathin ZIF-8 membrane taking assistance from graphene oxide (GO) nanosheets.[72] In their method, GO nanosheets were first added to the ZIF-8 precursor solution at room temperature. The ZIF-8 formed on the surface of nanosheets for some time to obtain the seeds, named seeds-x h (where x notes the synthesis time). Seeds-3h was suspended in methanol and spin-coated on the anodized aluminum oxide (AAO) substrate. Finally, the sample was immersed into the ZIF-8 precursor solution again to produce the final intergrown ZIF-8 membrane (Fig. 3). The SEM image showed the final ZIF/GO membrane is well-intergrown and free of pinholes. The thickness of the membrane was only 100 nm (Fig. 3). It was reported that the GO nanosheet facilitated ZIF-8 growth, especially at the interface between the film and the porous support, while at the same time restricting the diffusion of precursors into the support pores. In this way, GO nanosheets acted as a barrier for the entry of synthesis solution inside the support pores, which paved the way for the ultrathin membrane.

C. Electrochemical deposition

The precursors for MOF nucleation, metal ions and deprotonated linkers, are charged. This makes the electrochemical method attractive because it allows one to regulate heterogeneous nucleation on the desired substrate with the applied current and voltage.[56,64,67,85] This way, reaction kinetics can be controlled to a much greater extent compared to direct growth or seeded secondary growth.

In 2018, we described an approach to synthesize MOF membranes [Fig. 4(a)], where a seeded layer was first deposited on porous substrates by electrophoretic deposition within a few minutes [Fig. 4(b)].[63] Then, the nuclei film was left in the precursor solution for a short period of time to get the final well intergrown membranes [Fig. 4(c)]. This method was further developed for crystallization using sustained precursors (CUSP) in 2020.[97] In this way, a continuous precursor solution was spread on the same nuclei film from the previous approach at a constant rate while avoiding the transition to the Ostwald ripening stage, thus resulting in a uniform grain size. In the same year, Lai *et al.* presented aqueous cathodic

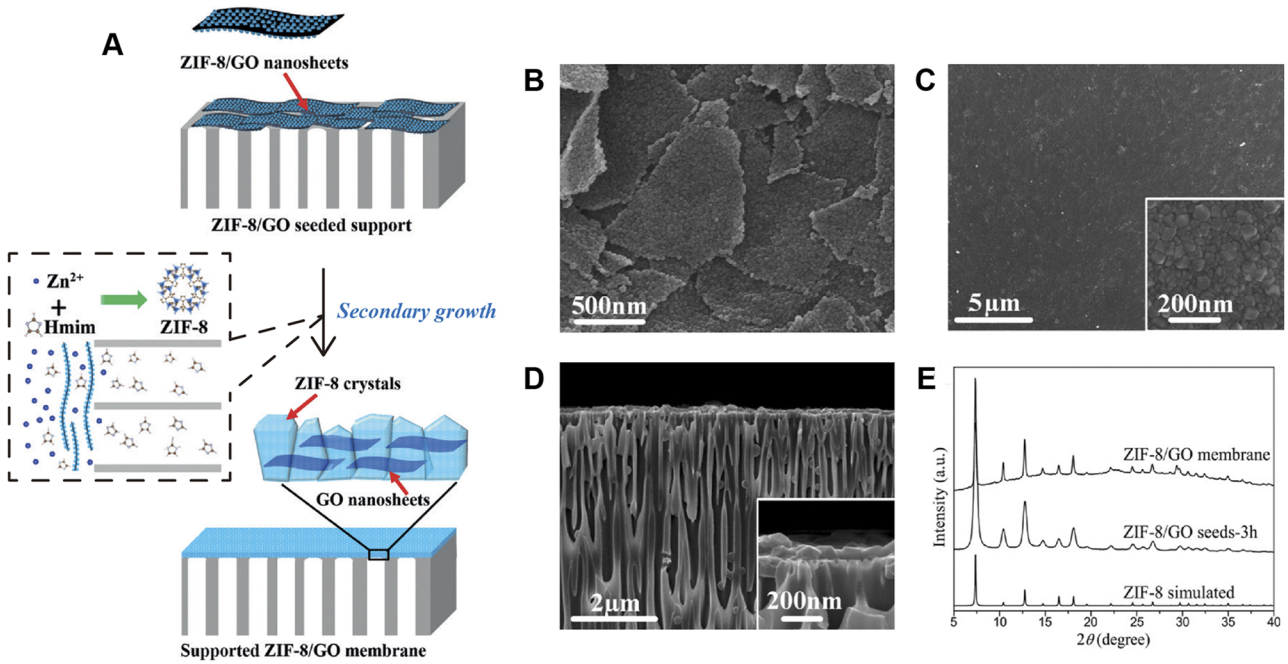

FIG. 3. (a) Schematic of secondary growth of ultrathin ZIF-8 membrane using 2D ZIF-8/GO hybrid nanosheets as seeds. (b) SEM image of seed powder and on-top view (c) and cross-section (d) of ZIF/GO membrane. (e) PXRD pattern of seeds-3h powder and ZIF/GO membrane.[72] Reprinted with permission from Hu *et al.*, Angew. Chem., Int. Ed. **55**(6), 2048 (2016). Copyright 2016 Wiley.

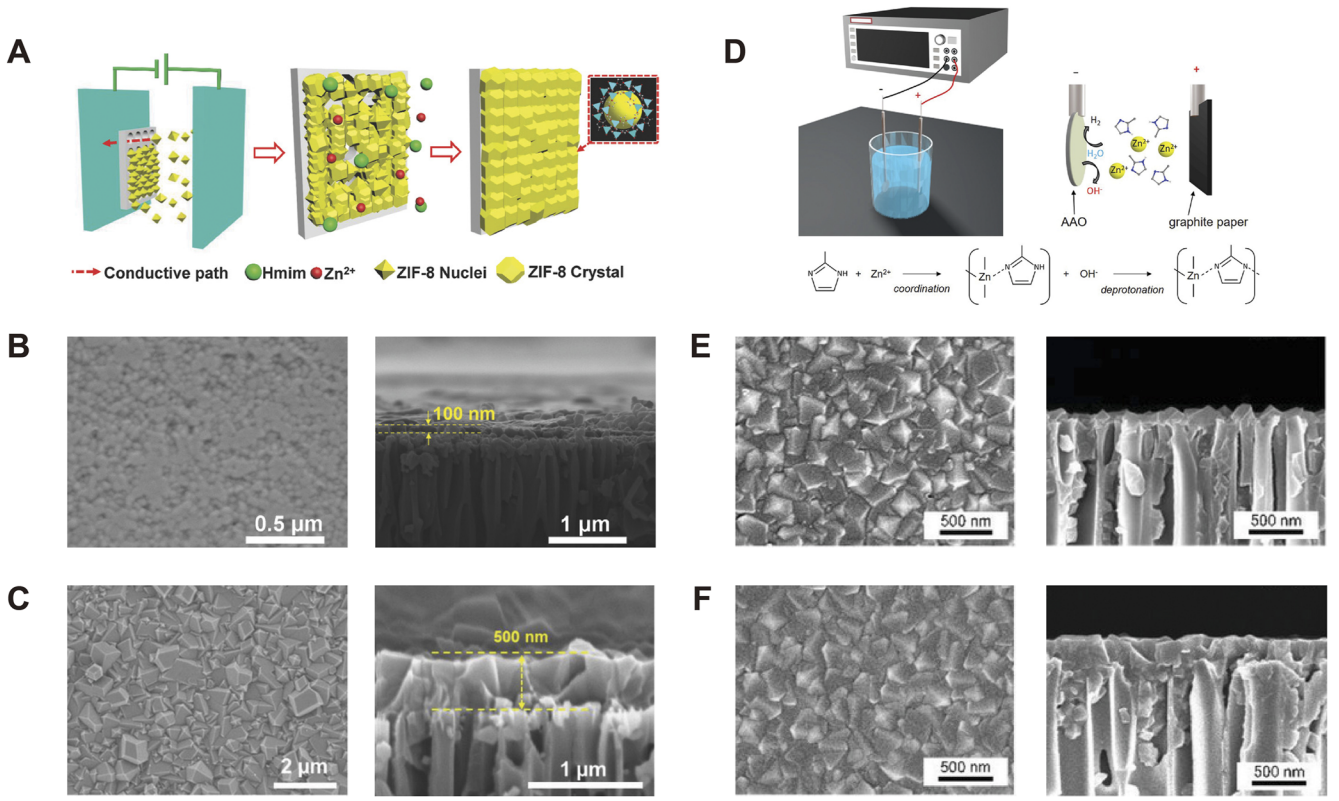

FIG. 4. (a) Schematic of the electrophoretic deposition process for the synthesis of MOF films. (b) and (c) SEM images and cross section of ZIF-8 nuclei and membranes on AAO support, respectively.[63] Reprinted with permission from He *et al.*, Adv. Funct. Mater. **28**(20), 1707427 (2018). Copyright 2018 Wiley. (d) Schematic of the ACD process for the synthesis of MOF films. (e) and (f) SEM images and cross section of ZIF-8 membranes synthesized at 30 and 40 min, respectively.[64] Reprinted with permission from Wei *et al.*, Adv. Funct. Mater. **30**(7), 1907089 (2019). Copyright 2019 Wiley.

deposition (ACD) of ZIF-8 membranes [Fig. 4(d)].[64] They directly fabricated ZIF-8 membranes on porous substrates by using a dilute precursor solution and low current without the addition of any supporting electrolyte or modulator. OH^- ions were detected from the reduction of water near the cathode, which is hypothesized to facilitate the deprotonation of the zinc–ligand complex near the substrate, thus helping the formation of membranes. The thickness of ZIF-8 membranes could be controlled by deposition time [Figs. 4(e) and 4(f)].

Eddaoudi *et al.* developed an electrochemical directed-assembly strategy to fabricate polycrystalline metal–organic framework films (Fig. 5).[85] In this method, the linker deprotonation rate was controlled by electrochemistry, which balanced nucleation and crystal growth for continuous membrane formation. In addition, ligand-to-cluster ratios also played an important role, where optimal ratios were reported for various structures. For example, a ratio of 5.6:1 provided a defect-free Y-fum-**fcu**-MOF membrane with a thickness of 85 nm (~45 unit cells) at a cluster concentration of 15 mM and a current density fixed at 1.5 mA cm^{-2}. By this method, a series of iso-reticular MOF membranes with different metals and linkers were fabricated, with a thickness ranging from 75 to 890 nm.

In a follow-up study, mixed linker Zr-fum-**fcu**-MOF membranes, where fumarate linker was partially (from 21% to 59%) substituted by mesaconate linker, were synthesized by the same electrochemical deposition method (Fig. 6).[56] Because of the extra methyl group in the mesaconate acid linker, the aperture of the MOF structure was changed from the original triangle to an asymmetric trefoil-shaped pore aperture, which effectively blocked the diffusion of CH_4 molecules because of a shape mismatch between them. While the linear molecules CO_2 and N_2 were unaffected, this provided an ideal pore shape for the separation of N_2 from CH_4.

D. Vapor deposition

Vapor deposition has been proven to be a useful strategy for the fabrication of ultrathin 2D materials such as single-layer graphene and metal dichalcogenides, which depend on the reaction of the vapors of the reactants, leading to a continuous and uniform morphology. Compared to conventional solution-based methods, the vapor deposition method is environmentally friendly, incurs a lower cost, and is easier to scale-up. Recently, this method has been introduced into the synthesis of ultrathin MOF membranes. Ameloot *et al.* developed one of the first chemical vapor depositions of ZIF thin films in 2016.[98] They first coated a layer of ZnO by

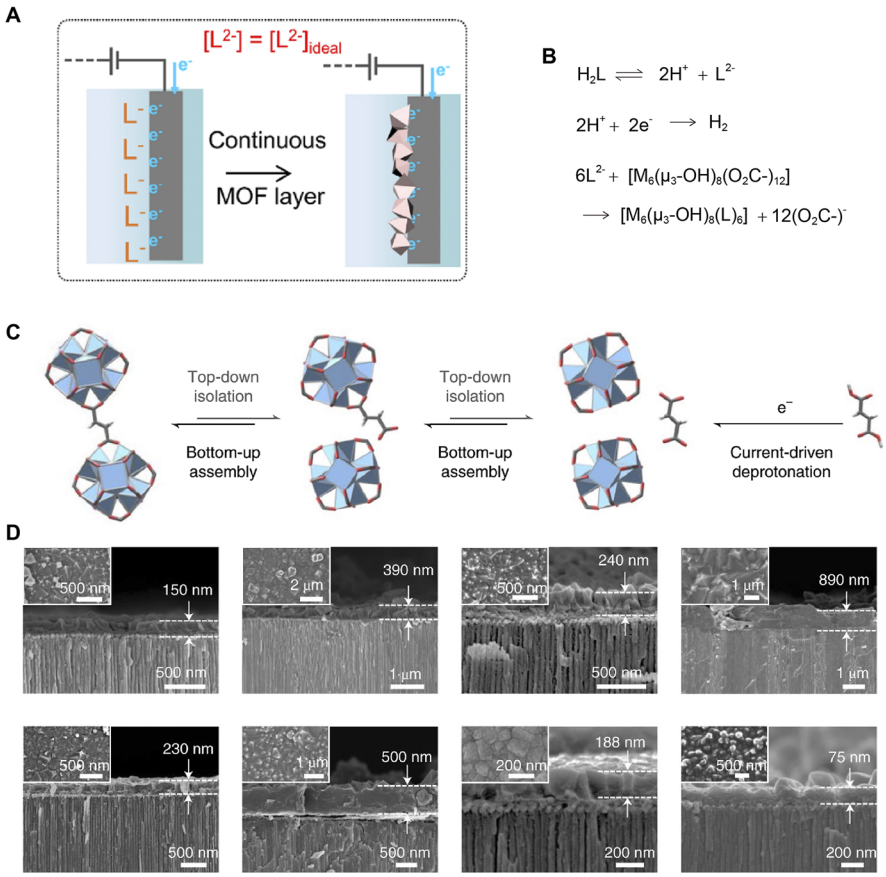

FIG. 5. Electrochemical directed-assembly strategy to fabricate polycrystalline metal–organic framework membranes. (a) Schematic of the synthesis of MOF membranes. (b) and (c) Illustration of control of equilibrium between protonated and deprotonated forms during the formation of MOF membranes. (d) SEM images of a series of **fcu**-MOF membranes.[85] Reprinted with permission from Zhou *et al.*, Nat. Energy **6**(9), 882 (2021). Copyright 2021 Springer Nature.

atomic layer deposition (ALD) on the substrate, followed by the reaction of ZnO with 2-methylimidazole (HmIm) vapor. The thickness of these MOF films could be controlled by the deposition time of ZnO. This method led to thin but smooth and continuous MOF films, which showed advantages in processability compared to the conventional solution-based method. Zhang *et al.* developed the gel-vapor deposition method to fabricate the ultrathin MOF membranes.[55] In this way, they combined the sol-gel coating to make a thin film for the metal precursor and introduced linker vapor to complete the reaction. The Zn based sol-gel was prepared by the reaction of zinc acetate dihydrate and ethanolamine in ethanol. This could be conveniently coated on a porous polymeric substrate, which yielded the gel precursor upon heating to 150 °C. Following this, HmIm vapor was introduced while the substrate was heated to react with gel to form the final ZIF-8 membrane [Fig. 7(a)]. SEM images confirmed the transformation of the morphology of the surface. They could achieve a well-intergrown ultrathin ZIF-8 layer by this method [Fig. 7(b)]. Furthermore, by tuning the synthesis time and concentration of Zn, they could tune the thickness of the membranes. The thinnest membrane was only 17 nm [Fig. 7(c)], representing one of the thinnest MOF membranes reported so far. This indicates the advantage of the vapor deposition method for the synthesis of ultrathin MOF membranes, which can fine-tune the thickness by controlling the deposition conditions, and the pre-deposited precursor will also guide the formation of continuous membranes. XRD of the powder based on the same method confirmed the crystal structure of ZIF-8. Similarly, Zhang *et al.* applied this method to the synthesis of an ultrathin layered $Co_2(bim)_4$ membrane,[68] where Co-based gel was dip-coated on the surface of a porous α-alumina tube, followed by treatment with benzimidazole vapor to get the final membrane. Before coating the Co-based gel, GO was utilized to smoothen and functionate the surface of porous α-alumina tubes. The thickness of the $Co_2(bim)_4$ membrane could be controlled by the dip-coating time of the Co-based gel, leading to 57–570 nm thick films. The resulting film was *c*-oriented based on the XRD measurements.

In 2018, Tsapatsis *et al.* reported an all-vapor-phase fabrication method to synthesize ultrathin ZIF-8 membrane.[58] Compared

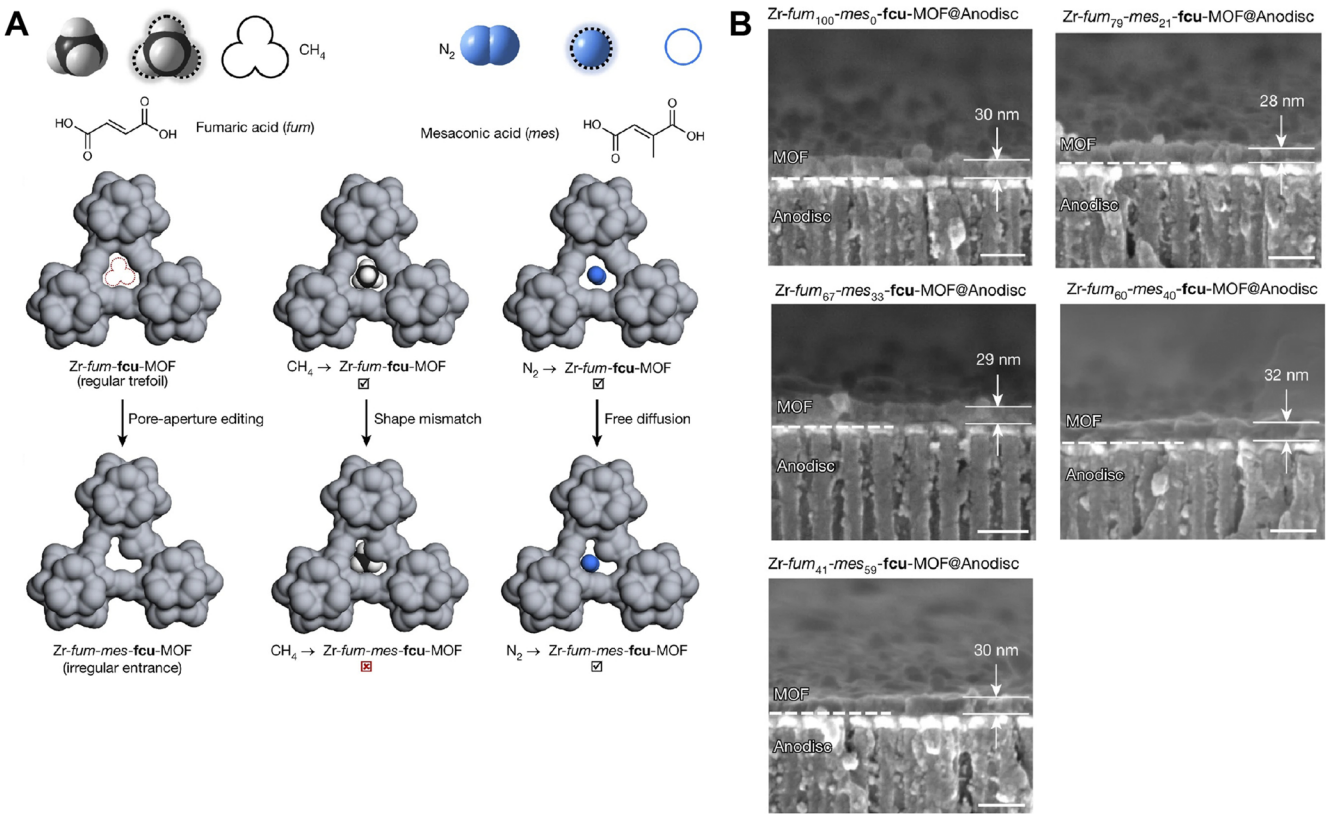

FIG. 6. (a) Illustration of pore aperture shape modification to block the diffusion of CH_4 molecule. (b) SEM images of mixed-linker Zr-*fum*-***fcu***-MOF with different linker ratios; scale bar is 100 nm.[56] Reprinted with permission from Zhou *et al.*, Nature **606**(7915), 706 (2022). Copyright 2022 Springer Nature.

to Zhang's work, it was solvent-free, and the precursors and resultant ZIF were filled in the pores of the substrate. This method is composed of two steps. First, diethylzinc was loaded on the surface of substrate alumina by atomic layer deposition, where diethylzinc reacted with introduced water to form zinc oxide and/or zinc hydroxide. Second, the sample was exposed to an HmIm gas atmosphere to get the final ZIF-8 membrane [Fig. 8(a)]. A high-angle annular dark-field scanning transmission electron microscopy (HAADF-STEM) image and corresponding energy-dispersive x-ray (EDX) based mapping of the cross-section were used to determine the morphology of the ZIF-8 membrane. These techniques were quite useful in resolving the interface of ultrathin film, which is a tough challenge. As expected, only the Al signal was detected in the substrate. Zn signal was obtained only after ZnO deposition, where it is present at the top 200 nm of the substrate [Fig. 8(c)]. In addition, after the formation of ZIF-8, the distribution of the Zn signal changed dramatically as Zn was mobilized during the HmIm-vapor treatment [Fig. 8(d)].

E. Interfacial synthesis

Interfacial growth has been a dominant technology for the fabrication of commercial polyamide nanofiltration (NF) and reverse osmosis (RO) membranes.[99] In this method, a microporous polymer substrate is exposed to an aqueous solution of amine monomer, followed by exposure to an organic solution of acyl chloride. The two monomers react on the surface of the substrate, forming a thin selective layer. Similar to the case of polyamide, for MOF films, there are also two precursors, metal ions and organic ligands. Motivated by this, interfacial growth has also been applied in the syntheses of MOF membranes.[53,69,70,100] In this regard, a porous substrate is treated with metal ion and organic ligand solutions, respectively, to form a thin MOF film, where the reaction kinetics are finely controlled by the concentration of precursors. Zhong *et al.* proposed an interface layer polarization induction approach in 2020.[70] A polymeric substrate was immersed in the methanol solution of metal ions and linkers, where the metal ions and organic linkers were adsorbed on the surface of the substrate, yielding an ultrathin MOF film [Fig. 9(a)]. Three different MOF membranes, ZIF-8, DZIF-8, and Cu-BTC, were obtained by this method. All could be prepared in ultrathin morphology, with thickness ranging from 58 to 110 nm. The structures of these MOF membranes were determined by XRD [Figs. 9(b)–9(d)]. As for DZIF-8, diethanolamine (DEA) was mixed with HmIm to make an isoreticular structure with ZIF-8 but containing more open metal sites, which favored gas separation.

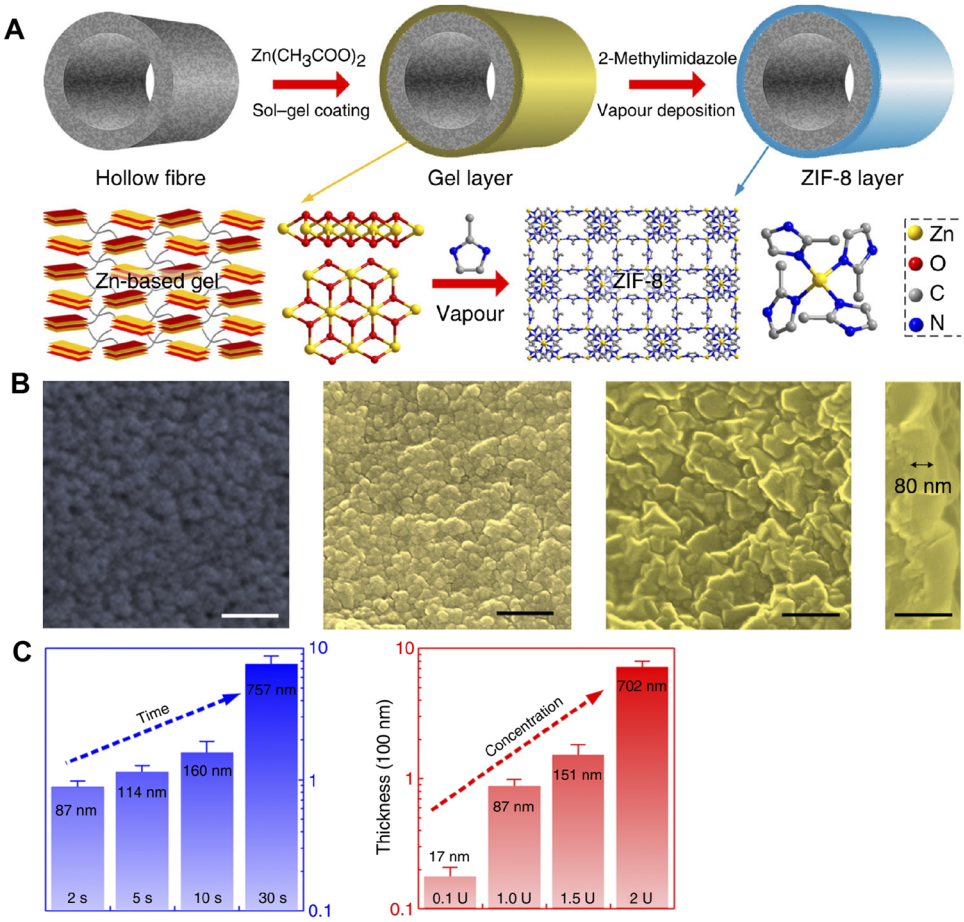

FIG. 7. Synthesis of the ultrathin ZIF-8 membrane by gel-vapor deposition. (a) Schematic of the method. (b) SEM images of substrate, Zn-based gel layer, and ZIF-8 membrane with cross-section image. Scale bar: 200 nm. (c) Thickness of ZIF-8 membranes prepared with different coating time and sol concentration.[55] Reprinted with permission from Li *et al.*, Nat. Commun. **8**(1), 406 (2017). Copyright 2017 Springer Nature.

Similar to interfacial growth, the contra-diffusion method was proposed to synthesize thin MOF membranes. Here, a porous substrate is placed between two precursors so they can react on the surface of the substrate to form a thin film. Compared to interfacial growth, only one cycle of synthesis is needed here. In this regard, Wang *et al.* carried out the synthesis of the ZIF-8 membrane with the assistance of modified carbon nanotubes (CNT) as a nano-scaffold.[101] Especially, CNTs coated with a layer of polydopamine (PDA) were vacuum-filtered onto an anodized aluminum oxide (AAO) disk. Following this, ZIF-8 membranes were synthesized on this substrate by the room-temperature contra-diffusion method with varying synthesis time [Fig. 10(a)]. The results showed ZIF-8 films were formed on top of modified CNTs and fully covered them after 60 min of reaction [Fig. 10(e)]. The resulting membranes were only 100–200 nm thick, yet they were well-intergrown and free of pinholes [Figs. 10(e) and 10(f)]. XRD of this ultrathin film matched well with the simulated pattern of ZIF-8 [Fig. 10(g)]. It is worth noting that the ZIF-8 film was formed only on one side of the support. This morphology results from the fine design of the substrate, where attractive hydrophobic interaction between the organic ligands and aromatic units at the top layer of PDA results favored the formation of the ZIF film.

F. Layer-by-layer deposition

The layer-by-layer strategy is a promising method for the fabrication of ultrathin membranes, where the thickness can be precisely controlled by the number of synthesis cycles. It is also an extremely scale-up friendly method, as layer deposition and washing can be carried out by an automated system. In 2017, Heinke *et al.* reported the preparation of a thin HKUST-1 membrane by a step-by-step spraying technique.[102] Solutions of copper(II) acetate and trimesic acid in ethanol, both with a concentration of 0.1 mM, were sprayed onto the AAO surface sequentially. Ethanol was used to rinse the sample in between the metal and organic linker deposition [Fig. 11(a)]. SEM images and energy-dispersive x-ray spectroscopy (EDS) mapping revealed a uniform film morphology [Fig. 11(a)]. A cross-sectional SEM image revealed that thickness after 100 cycles of spray was 450 nm [Fig. 11(b)], which then increased to 500 nm

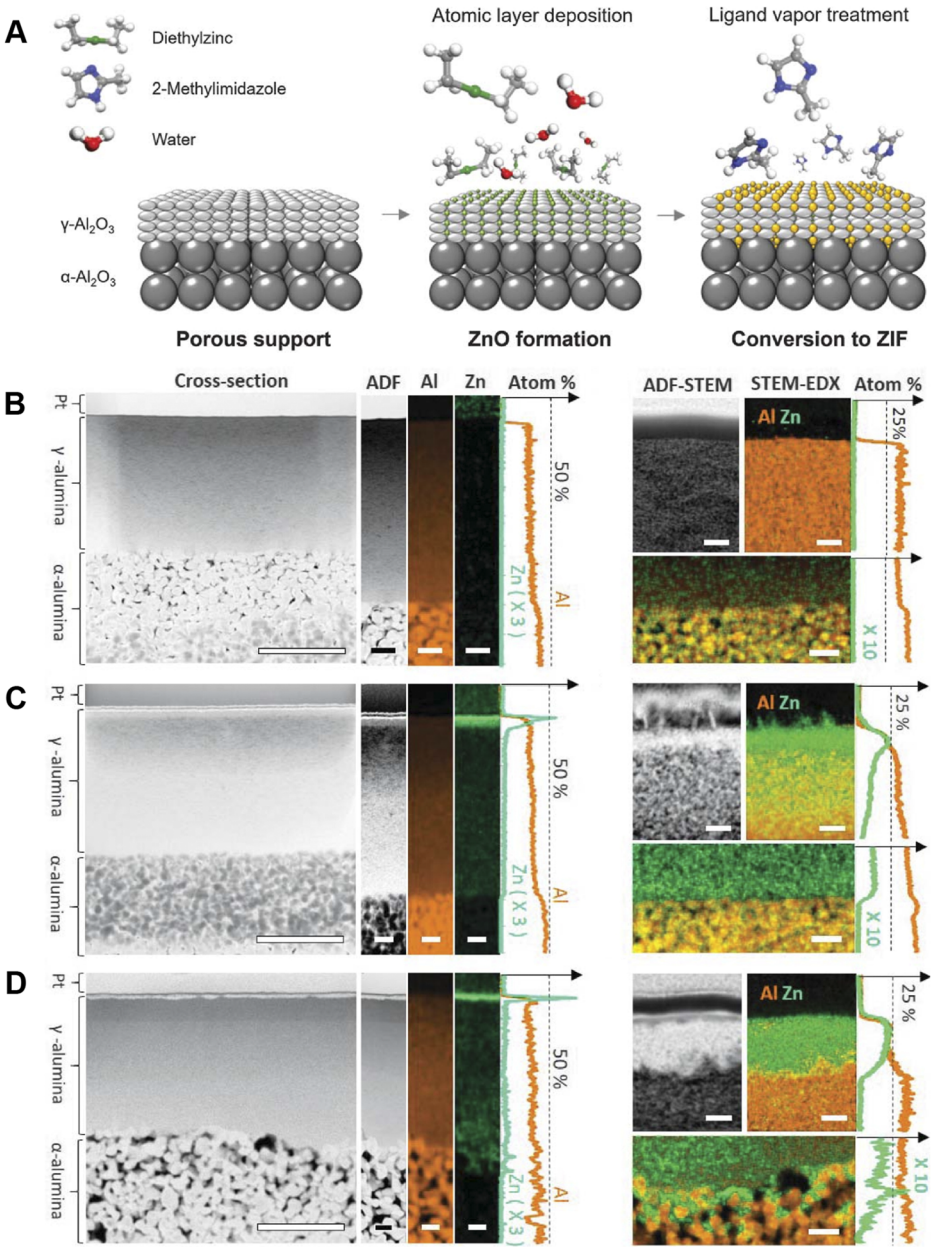

FIG. 8. Synthesis of ultrathin ZIF-8 membrane by all-vapor-phase fabrication. (a) Schematic of the process. ADF-STEM and EDX mapping of elements of the substrate (b), after ZnO deposition (c), and after MOF formation (d). (b) to (d) On the left, large scale bars, 2 mm; small scale bars, 400 nm; on the right, small scale bars (top), 50 nm; larger scale bars (bottom), 500 nm.[58] Reprinted with permission from Ma *et al.*, Science **361**(6406), 1008 (2018). Copyright 2018 AAAS.

after 150 cycles. HKUST-1 membrane with a size of 1.8 cm could be prepared by this method [Fig. 11(c)].

Wang *et al.* reported the synthesis of the ZIF-8 membrane by a repetitive spin-coating protocol.[52] In their method, Zn^{2+} was first mixed with g-C_3N_4 and spined-coated on the AAO substrate, followed by the spin-coating of HmIm. This process was repeated for 10 cycles, and the sample was heated at 60 °C overnight [Fig. 12(a)]. The final ZIF-8 membrane was 240 nm thick and highly crystalline [Figs. 12(b) and 12(c)].

G. Nanosheet stacking

2D MOF nanosheets or MOF platelets are advantageous for the construction of ultrathin membranes. This is because they can be

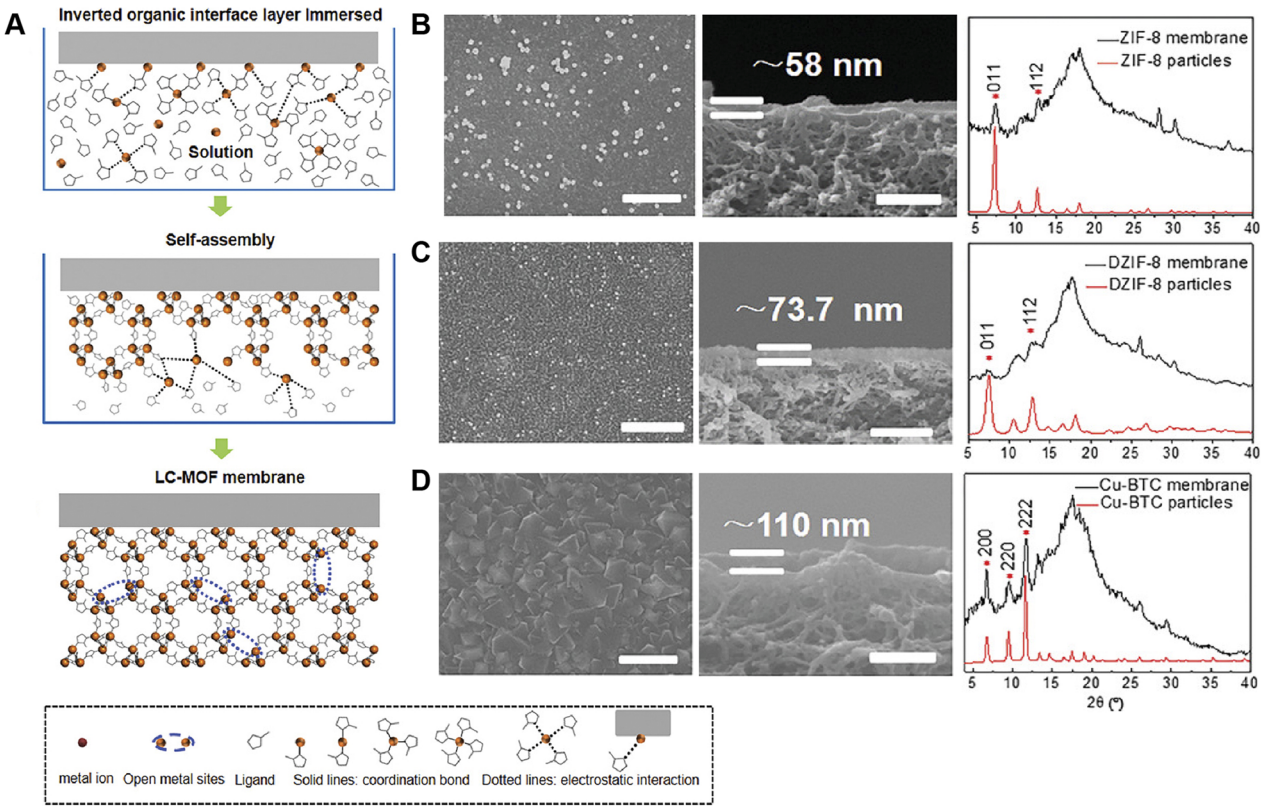

FIG. 9. Synthesis of ultrathin low-crystalline MOF membranes by interface layer polarization induction. (a) Schematic of the fabrication process. SEM image of the top view, cross-section, and XRD pattern of ZIF-8 (b), DZIF-8 (c), and Cu-BTC (d), respectively.[70] Reprinted with permission from Qiao *et al.*, Adv. Mater. **32**(34), e2002165 (2020). Copyright 2020 Wiley.

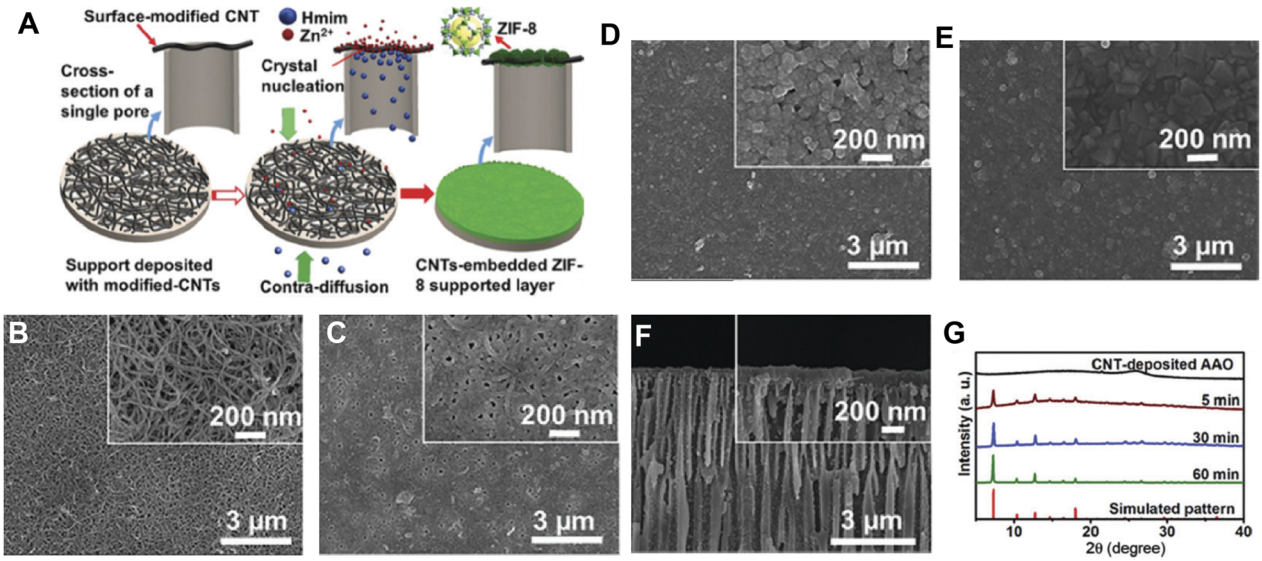

FIG. 10. (a) Schematic of fabrication of the ZIF-8 membrane by using modified CNTs as support. (b) SEM image of the modified CNT substrate. SEM images of ZIF-8 membrane grown for 5 min (c), 30 min (d), and 60 min (e) and (f), respectively. (g) PXRD pattern of each sample.[101] Reprinted with permission from Shamsaei *et al.*, Chem. Commun. **52**(95), 13764 (2016). Copyright 2016 Royal Society of Chemistry.

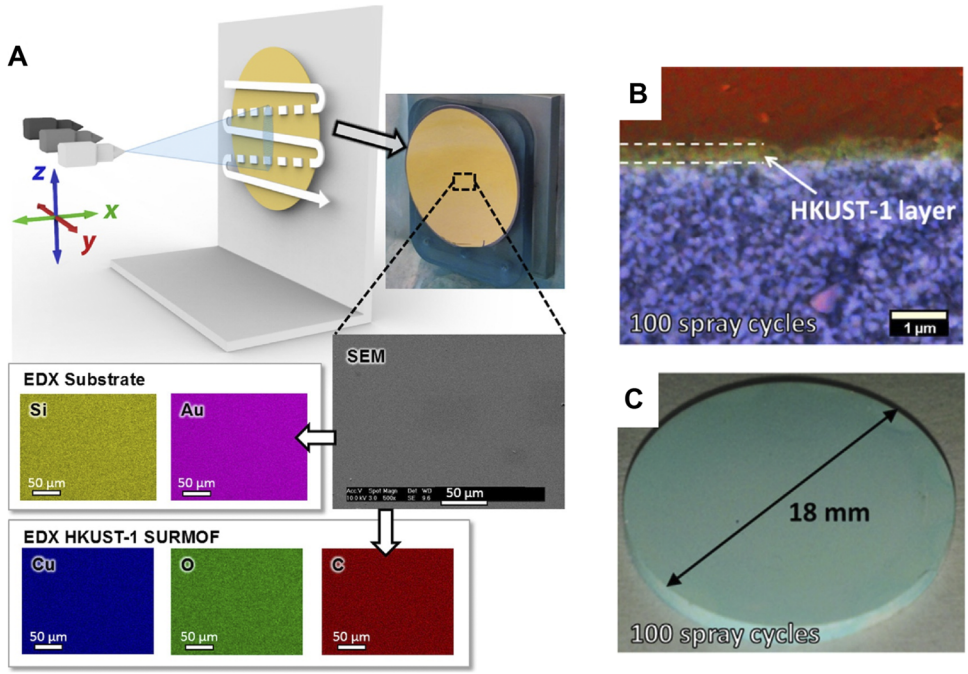

FIG. 11. Synthesis of the HKUST-1 membrane by the lay-by-layer method. (a) Schematic of the fabrication process, SEM image, and EDS mapping of the resultant HKUST-1 membrane. Cross-section SEM image (b) and photograph (c) of HKUST-1 membrane with 100 spray circles.[102] Reprinted with permission from Hurrle *et al.*, Chem. Eur. J. **23**(10), 2294 (2017). Copyright 2017 Wiley.

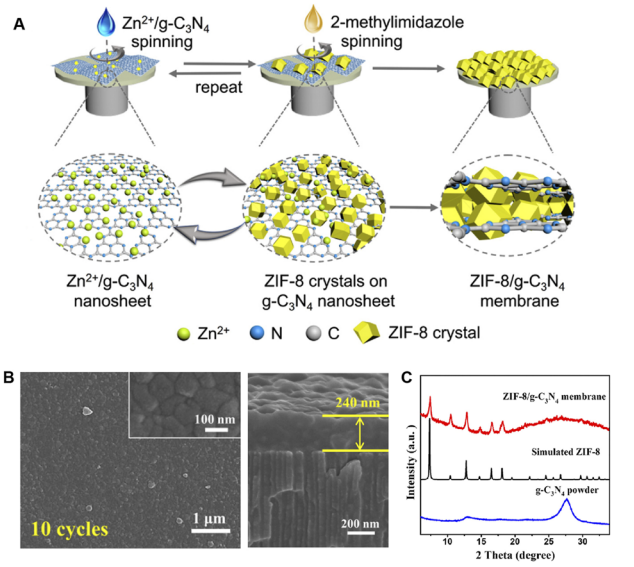

FIG. 12. (a) Illustration of the fabrication of an ultrathin ZIF-8 membrane by the layer-by-layer method. SEM image (b) and XRD (c) of the ZIF-8 membrane.[52] Reprinted with permission from Hou *et al.*, Chem. Eng. Sci. **182**, 180 (2018). Copyright 2018 Elsevier.

stacked in a compact film, thanks to their flexibility arising from a high aspect ratio. These nanosheets can be obtained by exfoliation of layered precursors by developing methods that can overcome van der Waals interactions, hydrogen bonding, and electrostatic interactions between neighboring layers. This is very attractive because individual monolayers can be as thin as those represented by a unit-cell parameter.[59,76,87,103,104] In 2014, Yang *et al.* exfoliated $Zn_2(bim)_4$ by wet ball-milling and ultrasonication to obtain monolayer nanosheets (Fig. 13). After that, a colloidal dispersion of these nanosheets was hot-dropped onto the surface of an α-Al_2O_3 disk to obtain an ultrathin film. XRD combined with SAED was used to confirm the crystal structure of the nanosheet [Fig. 13(d)]. The thickness of the nanosheet was 1.12 nm based on the AFM data [Fig. 13(e)].[59] This method is versatile and attractive to synthesize a number of 2D MOF nanosheets, such as $Zn_2(bim)_3$,[87] MAMS-1,[103] Nx-$Zn_2(bim)_4$,[104] etc. Wang *et al.* also synthesized Al-MOF and exfoliated the nanosheets by sonication to get nanosheets. This facile exfoliation from the 3D structure of Al-MOF may come from some defects in its one-dimensional (1D) Al-oxo building block.

Exfoliation-based nanosheet preparation is limited to those structures that can be synthesized in layered morphology. Non-layered MOFs have been recently synthesized as thin nanosheets by direct bottom-up approach. For example, thin nanosheets of a NH_2-MIL-53(Al) and ZIF-8 were obtained by a surfactant-assisted[76,105] synthesis approach. Gascon *et al.* used a cationic

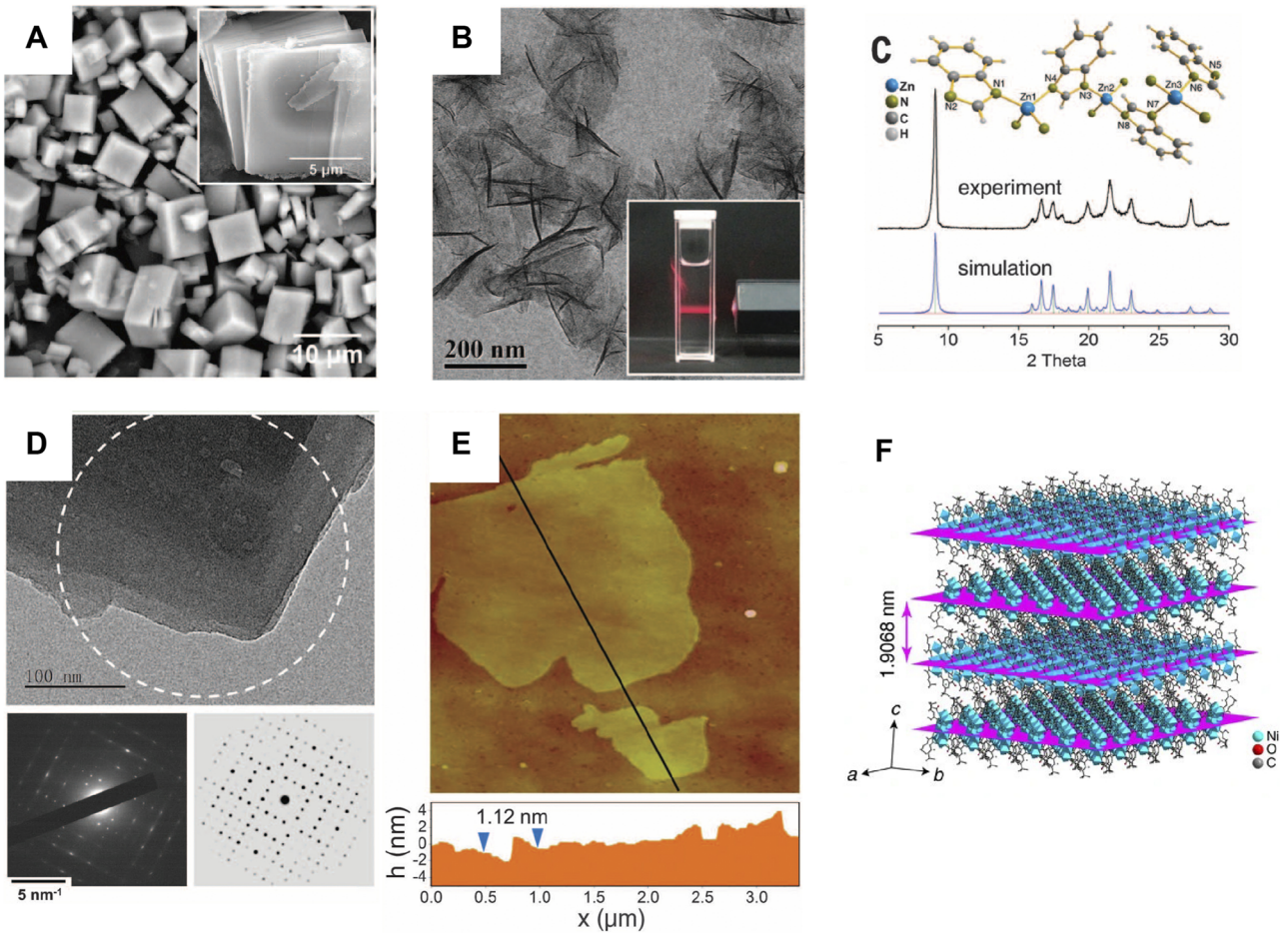

FIG. 13. Fabrication of ultrathin MOF membranes by exfoliation of nanosheet. (a) SEM image of as-synthesized $Zn_2(bim)_4$ crystals. (b) TEM image of the $Zn_2(bim)_4$ nanosheet. The inset shows the Tyndall effect of a colloidal suspension. (c) PXRD pattern of the $Zn_2(bim)_4$ nanosheet compared to simulation. (d) SAED pattern (white circle) of $Zn_2(bim)_4$ nanosheet and corresponding simulated pattern. (e) AFM image and corresponding height profile of $Zn_2(bim)_4$ nanosheet.[59] Reprinted with permission Peng *et al.*, Science **346**(6215), 1356–1359 (2014). Copyright 2014 from AAAS. (f) Crystal structure of MAMS-1.[103] Reprinted with permission Wang *et al.*, Nat. Commun. **8**, 14460 (2017). Copyright 2017 from Springer Nature.

surfactant, cetyltrimethylammonium bromide (CTAB), to pre-organize metal ions into an oligomeric structure and then introduced the organic linker to obtain the platelet morphology [Fig. 14(a)]. Small-angle X-ray Scattering (SAXS) was applied to obtain insights into the formation mechanism of the structure. A quasi-Bragg peak at $q = 1.6\ nm^{-1}$ for the CTAB-treated Al^{3+} system was observed, indicating stacking of nanosheets [Fig. 14(b)]. Interestingly, this peak vanished after the addition of the linker, which was attributed to the formation of the NH_2-MIL-53(Al) nanosheet by the perturbation of the Al^{3+}-CTAB system. CO_2 adsorption, TEM, and XRD were used to confirm the crystal structure. High-resolution TEM (HRTEM) and SAED of the sample confirmed the presence of 1D pores perpendicular to the nanosheet [Fig. 14(c)]. By using the same method, they successfully synthesized another MOF, NH_2-CAU-10(Al). We recently synthesized ZIF-8 nanosheets using sodium dodecyl sulfate (SDS) as a surfactant.[105] The morphology of the resultant ZIF-8 nanosheet was controlled by the synthesis temperature and time, where 40 °C and 3.5 h were found to be optimal. XRD and SAED were performed to confirm the crystal structure of the ZIF-8 nanosheet. AFM was used to determine the thickness of the nanosheet (about 40 nm). The membrane was fabricated by directly filtering the growth precursor solution containing nanosheet without any further purification or treatment of the precursor, resulting in a *c*-out-of-plane-oriented film on a porous substrate, as confirmed by XRD. This approach greatly minimizes the number of processing steps and reduces waste in the synthesis of membranes.

H. Postsynthetic modification

Postsynthetic modification can be applied to fine-tune the crystal structures of MOF membranes, which can then be used

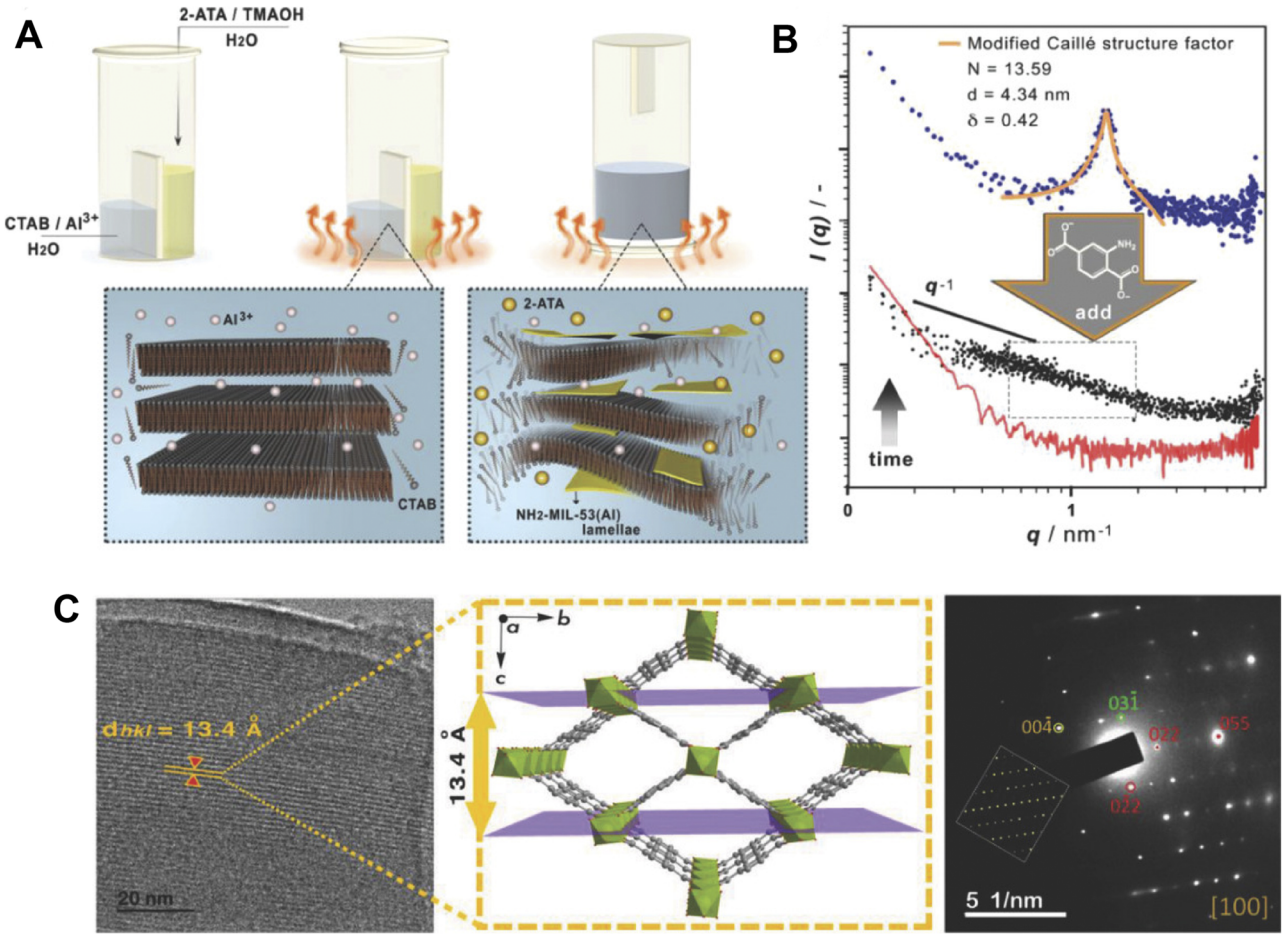

FIG. 14. (a) Illustration of the synthesis of the NH_2-MIL-53(Al) membrane by a bottom-up surfactant-assisted synthetic approach. (b) SAXS patterns acquired at 373 K for an aqueous solution of CTAB and $Al(NO_3)_3{\cdot}9H_2O$ before and after adding the deprotonated linker (blue and black points, respectively). (c) HRTEM image and SAED pattern of NH_2-MIL-53(Al) nanosheet.[76] Reprinted with permission from Pustovarenko *et al.*, Adv. Mater. **30**(26), e1707234 (2018). Copyright 2018 Wiley.

to tune the separation performance. This is one of the strong advantages of MOFs compared to other porous materials, e.g., zeolite. Jeong *et al.* reported this method to decrease the effective thickness of MOF membranes.[79] They first synthesized a 1-μm-thick ZIF-8 membrane using a counter-diffusion-based *in situ* method. Next, they solvothermally treated the membrane with a 2-imidazolecarboxaldehyde (Ica)/methanol solution at 60 °C for 1–4 days to get the final Ica-CD-ZIF-8 membrane. Due to the smaller size of Ica compared to HmIm, the effective pore aperture of Ica-CD-ZIF-8 is 5.0 Å, in contrast to 4.0 Å for as-synthesized ZIF-8. As a result, the Ica-CD-ZIF-8 layer was not the selective layer for gas separation; however, it increased the overall gas flux. By controlling the exchange process, the thickness of the selective ZIF-8 layer could be tuned to a value significantly smaller than 1 μm [Fig. 15(a)]. This method is attractive because it allows thickness modulation for the selective layer without changing the crystallinity of the MOF film [Figs. 15(b) and 15(c)].

Although several strategies for the fabrication of MOF membranes can be used to synthesize ultrathin MOF membranes, some of them are advantageous, while others are disadvantageous in terms of conditions and criteria. As for the thickness, vapor deposition and nanosheet stacking provide thinner membranes compared to others (Table I). This may come from the intrinsic design of these experiments, where the vapor deposition method is based on vapor. Vapor concentrations can be quite dilute while maintaining a homogeneous distribution of reactions. This aspect is difficult to realize in solution-based syntheses. As for nanosheet stacking, it is based on nanosheets of MOF crystals, which have a thickness down to one unit-cell, i.e., a few nanometers. Therefore, continuous membranes can be formed by stacking a few layers, resulting in ultrathin MOF membranes. As for defect control in polycrystalline MOF membranes, a key challenge is understanding and controlling the contribution of grain boundaries to molecular transport. All of the above-discussed methods have the potential to control defects,

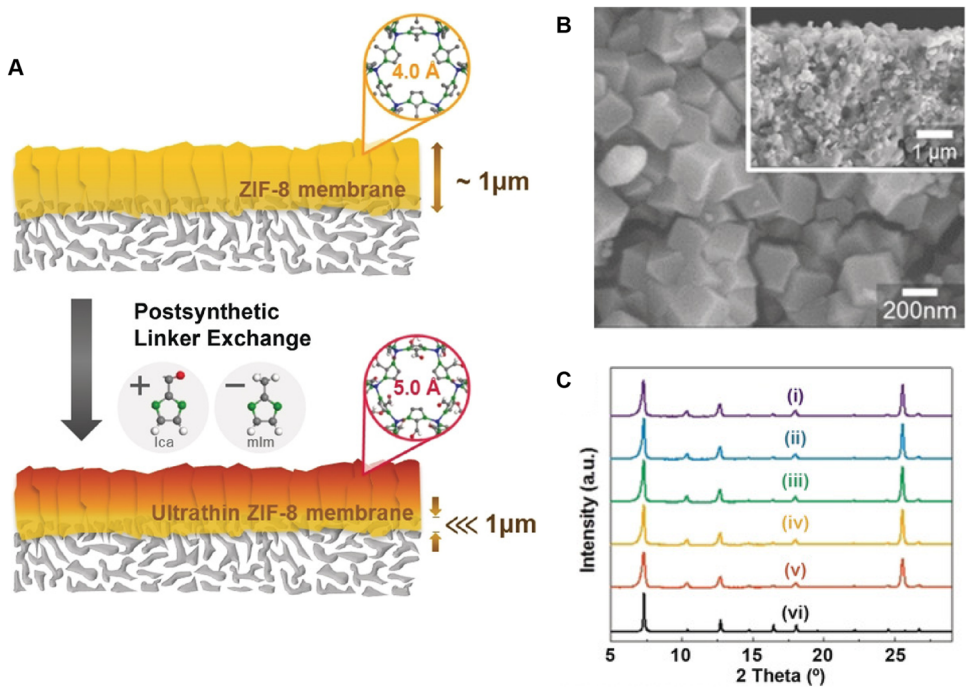

FIG. 15. (a) Schematic of the synthesis of ultrathin ZIF-8 membrane by the postsynthetic linker exchange method. SEM image (b) and XRD data (c) of the final Ica-CD-ZIF-8 membrane.[79] Reprinted with permission from Lee *et al.*, Angew. Chem., Int. Ed. **57**(1), 156 (2018). Copyright 2018 Wiley.

e.g., by extending synthesizing time and/or by increasing precursor concentration. Similarly, an extension of deposition cycles is also usually applied in deposition methods to control defects. For the electrochemical route, this can be realized by increasing the current. All of these routes have a trade-off; that is, they will lead to a thicker membrane. Nevertheless, the "Holy Grail" for the fabrication of ultrathin MOF membranes is single layer MOF film, akin to two-dimensional materials such as graphene, with a large area of

TABLE I. Comparison of conditions and criteria for the fabrication of ultrathin MOF membranes.

	Thickness	Defect control	Scalability	Solvent	Generality	References
Direct synthesis	≥50 nm		Easy	Water/organic solvent	Yes	54, 89–95
Seeded secondary growth	≥100 nm	Extension of synthesis time/increase of concentration of precursors	Difficult	Water/organic solvent	Yes	62, 72, and 96
Interfacial synthesis	≥58 nm		Easy	Water/organic solvent	Yes	53, 69, 70, and 99–101
Postsynthetic modification	Tens of nanometers		Difficult	Water/organic solvent	No	79
Nanosheet stacking	≥10 nm	Extension of deposition cycles/increase the concentration of nanosheets	Difficult	Water/organic solvent	No	59, 76, 87, and 103–105
Layer-by-layer deposition	≥240 nm	Extension of deposition cycles/increase the concentration of precursors	Easy	Water/organic solvent	Yes	52 and 102
Vapor deposition	≥17 nm		Easy	No solvent	No	55, 58, 68, and 98
Electrochemical deposition	≥30 nm	Extension of synthesis time/increase of concentration of precursors/ increase of the current	Easy	Water/organic solvent	Yes	56, 63, 64, 67, 85, and 97

single crystal domain. Such a material will have much reduced grain boundaries. This may be realized by fine-tuning the syntheses conditions and crystallization kinetics inspired by the synthesis of layered MOF.

In terms of versatility to synthesize many kinds of MOF structures, the nanosheet stacking approach is only suitable for 2D structures, and the vapor deposition method requires a low sublimation temperature. However, the solvent-free nature of vapor deposition also makes it easy to scale up. The postsynthetic modification method is based on the functionalization of organic linkers or metal ions in the structures of present MOF membranes, which is also limited by those structures with similar organic linkers or metal ions. Theoretically, other methods including direct synthesis, seeded secondary growth, interfacial synthesis, layer-by-layer deposition, and electrochemical deposition can be applied in the synthesizing of several MOF structures into permselective membranes. However, there are only a few MOF structures that have been fabricated into ultrathin membranes, although there have already been more than 100 000 structures reported to date. One of the reasons behind this is that several MOFs have a large pore size, which limits their application in separations where the addition of expensive MOFs brings value in terms of performance gain. The second reason is that several MOFs are synthesized at high temperature and pressure, which hinders their synthesis in the form of ultrathin pinhole-free films on a porous support. Therefore, more efforts are needed to develop generic synthetic methodology for the fabrication of ultrathin MOF membranes.

III. APPLICATIONS OF ULTRATHIN MOF FILMS

A. Ultrathin MOF films in gas separation application

Ultrathin MOF films are attractive for gas separation because the low thickness of the selective layer promotes gas permeance, as shown in Fig. 16. A trend can be observed for H_2 and C_3H_6 permeances and for H_2/CO_2 and C_3H_6/C_3H_8 separations as a function of the film thickness. The letters in Fig. 16 correspond to references, as mentioned in the figure caption. However, this trend is not an entirely straightforward relationship between thickness and permeance. This is because pinholes and grain boundary defect populations also dictate gas permeance, which is often described qualitatively. In this section, we present a summary of the challenges and performance of ultrathin MOF films (less than 500 nm thick) toward various gas separations, including carbon capture (CO_2/N_2), hydrogen purification (H_2/CO_2), and propylene/propane separations (C_3H_6/C_3H_8).

The mechanism by which selective gas transport is achieved from MOF films varies based on the MOF structure and composition and the properties of the involved gases. For H_2 purification from larger molecules, MOFs offering molecular sieving potential are used. Here, one exploits the diffusivity cutoff based on the size of the pore aperture and molecule. This is typically observed for MOFs with small and rigid pores such as $Zn_2(bim)_4$, $Zn_2(bim)_3$, and MAMS-1, as illustrated in Fig. 1.

In the case of CO_2, a combined effect of diffusion and sorption selectivity determines the separation performance. Examples include lattice-stiffened ZIF-8, UiO-66, KAUST-7, and KAUST-8. For C_3H_6/C_3H_8 separation from ZIF-8, kinetic separation is achieved. Essentially, the flexible lattice of ZIF-8 accommodates both gases, which are larger than the crystallographically determined diameter of ZIF-8. However, C_3H_6 has a higher diffusivity in ZIF-8 than that for C_3H_8, thanks to the smaller cross-sectional area of the former.

1. Post-combustion carbon capture

Energy-efficient and low-cost CO_2 removal from flue gas has emerged as one of the most important problems in a bid to reduce the carbon emission footprint and limit climate change.[109] By capturing and storing CO_2 emissions from various industrial processes, including power generation and cement manufacturing, carbon

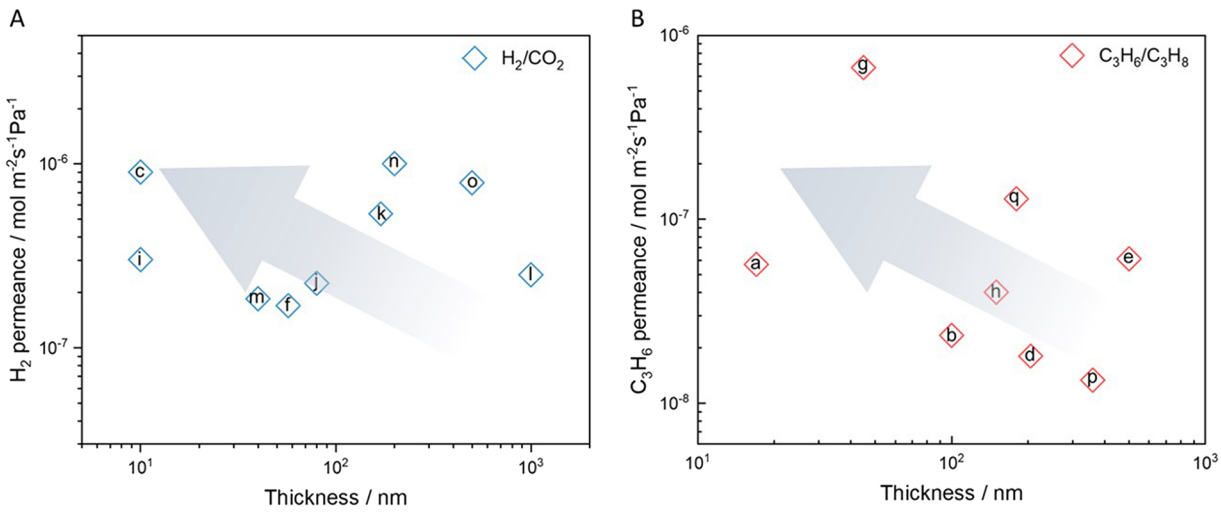

FIG. 16. Observed thickness-permeance relationship in the reported ultrathin MOF membranes, and the blue and red rhombuses represent the MOF films for (a) H_2/CO_2 and (b) C_3H_6/C_3H_8 separations, and the letters a to q in the figure correspond to the Refs. 55, 58–60, 63, 64, 68, 70, 85, 87, 106–107, and 108, respectively.

capture has the potential to significantly reduce greenhouse gas emissions and help limit the impact of climate change. For carbon capture applications, commercial amine-based absorption has a high energy requirement to strip the absorbed CO_2 and regenerate the solvent (from 3 to 4 MJ/kg_{CO2})[110] and a large capture penalty for the scale-up facilities (48–111 $/ton_{CO2}$).[111,112] In contrast, membrane-based separation has been shown to cut down on this cost because membranes do not rely on thermal energy. Attractive savings can be achieved using high-performance membranes. However, diffusion-driven separation of these two species is particularly challenging, given their similar kinetic diameters [$d(CO_2)$ = 3.3 Å and $d(N_2)$ = 3.64 Å]. Fortunately, CO_2 has a powerful quadrupole moment that provides a way for separation through chemical attraction (selective adsorption) instead of just relying on molecular size (selective diffusion). In this aspect, certain ultrathin MOF films have been investigated for carbon capture, and some of them fulfill the separation criteria through either adsorption-based selectivity, diffusion-based selectivity, or a combination of both.

Table II summarizes the top-performing ultrathin MOF films for carbon capture-based separations. Top-performing films to date involve polycrystalline films of KAUST-7 on KAUST-8,[67] lattice stiffened ZIF-8,[113] and (111)-oriented UiO-66.[62] In the subsequent paragraphs, we explain these membranes in detail.

A pivotal approach in the advancement of MOF membranes for post-combustion carbon capture lies in achieving a robust molecular sieving effect between CO_2 and N_2. Among the potential MOF candidates, ZIF-8 stands out, with an aperture size of ~3.4 Å, strategically positioned between the sizes of CO_2 (~3.30 Å) and N_2 (~3.64 Å). However, the occurrence of a "gate opening" effect leads to an enlargement of the pore size, resulting in a relatively modest CO_2/N_2 selectivity of only about 5.[114] Our group first reported a postsynthetic rapid heat treatment (RHT) method to stiffen the lattice.[113] After a few seconds of treatment at 360 °C, the ZIF-8 membrane exhibited unprecedented CO_2/CH_4, CO_2/N_2, and H_2/CH_4 selectivities exceeding 30, 30, and 175, respectively, and complete blockage of C_3H_6. Another study fabricated the (111)-oriented UiO-66 membranes by secondary growth using nanosheets as the seed layer.[62] They first created uniform triangular-shaped UiO-66 nanosheets that were 40-nm-thick using an anisotropic etching method. By implementing confined counter-diffusion-assisted epitaxial growth, they were able to create a highly (111)-oriented 165-nm-thick UiO-66 membrane. The framework's significant reduction in thickness and diffusion barrier contributed to the membrane's CO_2 permeance of 2070 gas permeation units or GPU (1 GPU = 3.35×10^{-10} mol m^{-2} s^{-1} Pa^{-1}) and CO_2/N_2 selectivity of 35.4.

An alternative approach for CO_2 separation involves harnessing the CO_2-philic groups within the MOF structures. Recently, the fluorinated metal-organic framework (KAUST-7) membrane, wherein the pyrazine linkers have great potential for strong CO_2 adsorption behavior, has been fabricated via *in situ* secondary growth.[67] The selectivities for CO_2/N_2, CO_2/H_2, and CO_2/CH_4 were 375, 60, and 175, respectively, and the film also showed tolerance to H_2S and water vapor. The KAUST-7 film, which was 800 nm thick, was fabricated using secondary growth on the KAUST-8 seed layer and was smoothened by vapor-assisted treatment. The excellent CO_2 separation performance was attributed to the optimal combination of adsorption affinity and molecular sieving. Given the remarkable reported selectivity and the unique CO_2-recognition behavior, further studies on this MOF would be of interest to uncover the mechanism underlying these findings and to improve the CO_2 permeance of this MOF.

Overall, for post-combustion carbon capture, the reported pure MOF membranes are listed in Table II. Top-performing films to date involve polycrystalline *in situ* growth films of KAUST-7 on KAUST-8, lattice stiffened ZIF-8, and (111)-oriented UiO-66. However, to date, there has been no reported MOF membrane where a sharp cut-off between CO_2 and N_2 molecules has been reported. Therefore, the synthesis of a suitable MOF film for CO_2 separation remains highly attractive for post-combustion capture.

2. Hydrogen purification

A modern method of power generation, distinct from the traditional approach of directly burning fossil fuels, involves reforming fossil fuels or biomass into hydrogen. After reforming and the water-gas shift reaction, the gas composition is close to 56% H_2, 40% CO_2, and small quantities of other gases, such as CO and H_2S, depending on the nature of the fossil fuel. The temperature of this gas for the low-temperature water-gas shift reaction is usually between 200 and 300 °C. Membranes can be used in this process to capture CO_2 from this stream to realize a pure stream of H_2, which can then be used as an emission-free fuel for a power plant. Therefore, this separation is also referred to as precombustion capture. Hydrogen-selective membranes can also be used to perform other separations such as modifications of the syngas ratio.

Table III summarizes the literature on ultrathin MOF films that have been reported for H_2/CO_2 separation. ZIFs[59,68,87,106,115] and

TABLE II. CO_2-selective ultrathin MOF membranes.

MOF	Highlight	Thickness (nm)	T (°C)	Pressure (atm)	Gas pair	Permeance (GPU)	Separation factor	Reference
KAUST-7&8	Strong CO_2 adsorption with pyrazine linker	~800	25 25	1 1	CO_2/N_2 CO_2/H_2	50 80	375 60	67
RHT-ZIF-8	Lattice stiffening via rapid heat treatment	550	25	1	CO_2/N_2	104	30	113
UiO-66	111 oriented stacked UiO-66	~200	25	1	CO_2/N_2	2070	35.4	62

TABLE III. Hydrogen separation performance of ultrathin MOF films.

MOF	Highlight	Thickness (nm)	T (°C)	Pressure (atm)	Gas pair	Permeance (GPU)	Separation factor	Reference
Cu-TCPP	Cu-TCPP on ZnO buffer layer	80	450	1	H_2/CH_4	671	50	116
MIL-96	*c*-oriented	170	25	1	H_2/CO_2	1600	12.6	117
ZIF-95	Solvent-free secondary growth	1000	100	1	H_2/CO_2	746	184	115
$Co_2(bim)_4$	Vapor phase transformation from Co gel to $Co_2(bim)_4$	57–750	30	1	H_2/CO_2	507	58.7	68
$Zn_2(bim)_4$	Wet ball milling of exfoliation, hot drop-coating	~10	200	1	H_2/CO_2	2700	291	59
MAMS-1	Freeze-thaw process of solvents of exfoliation, hot drop-coating	4–40	20	1	H_2/CO_2	553	235	118
$Zn_2(bim)_3$	Hot drop-coating	~10	160	1	H_2/CO_2	~900	166	87
UiO-67	Light-responsive azobenzene doped	~200	25	1	H_2/CO_2	~3000	8	107
ZIF-95	Vapor assisted in-plane growth	500	100	1	H_2/CO_2	2358	32.2	106

their derivatives have exhibited high performance in this regard. Moreover, several other MOFs, such as Cu-TCPP,[116] MIL-96,[117] and MAMS-1,[118] demonstrate high performance as well. We briefly summarize ultrathin MOF films for hydrogen purification below.

An effective strategy for H_2 separation involves introducing small molecules as dopants into the large pores. This dopant approach serves to reduce the pore size, enabling selective sieving of H_2 from an H_2/CO_2 mixture. Caro *et al.* developed a smart membrane with tunable gas permeation by depositing a 200-nm-thick UiO-67 film onto a porous α-Al_2O_3 support using solvothermal growth.[107] The UiO-67 membrane was loaded with light-responsive azobenzene (AZB) as guest molecules in its pores. The researchers demonstrated that by *in situ* thermally controlling the desorption of AZB from the membrane, light-induced gate opening and closing would happen, and the gas permeation could be altered. The UiO-67 membrane yielded H_2/CO_2 selectivity of 8 and H_2 permeance over 3000 GPU. This uncomplicated and effective technique resulted in a light-responsive membrane with controllable gas permeation.

Certain MOF structures exhibit a distinctive H_2 sieving effect within specific facets. By fabricating a facet-oriented MOF membrane that is selectively permeable to H_2, we can push the separation performance of this material to its maximum potential. Huang *et al.* reported a c-oriented ZIF-95 membrane via a vapor-assisted method.[106] By exposing a 500-nm-thick *c*-oriented ZIF-95 seed layer to a DMF/H_2O atmosphere, they could obtain in-plane film growth that maintained the same thickness as the seed layer. Because of the unique pore size of the ZIF-95 along the *c*-axis (~0.29 nm), the *c*-oriented ZIF-95 film displayed superior separation performance, with H_2/CO_2 and H_2/CH_4 selectivities of 32.2 and 53.7 and H_2 permeance of 2358 GPU. This concept was further extended to eliminate the grain boundaries between ZIF-95 nanosheets.[115] By grinding and adding the reactant powder to the seed layer without solvent, a 1-μm-thick film became defect-free. The oriented ZIF-95 exhibited an enhanced H_2/CO_2 selectivity of 184, with an H_2 permeance of 746 GPU. Liu *et al.* developed a highly *c*-oriented Cu-TCPP composite film through *in situ* growth on a layered double hydroxide (LDH) based ZnO buffer layer.[116] The ZnAl–NO_3 LDH was initially synthesized on a γ-Al_2O_3 substrate via a hydrothermal reaction, followed by calcination to form a ZnO buffer layer. The resulting 80-nm-thick Cu-TCPP layer exhibited a layered stacking along the c-axis, resulting in a narrow pore size (~5.4 Å) and interlocked interlayer gallery. The membrane showed excellent molecular sieving separation performance, with H_2/CH_4 selectivity of 50 and H_2 permeance of 671 GPU. Moreover, they extended their work to fabricate a highly *c*-oriented, well-intergrown ultrathin porous membrane. For this, they used monodispersed MIL-96 nanosheet seeds with a trace amount of polyvinyl pyrrolidone (PVP) in the seed suspension to avoid aggregation and N-dimethyl formamide (NMF) as a solvent during secondary growth. The resulting MIL-96 membrane was 170-nm-thick with a *c*-oriented microstructure and demonstrated an H_2/CO_2 selectivity of 12.6 and an H_2 permeance over 1600 GPU.

An alternative method for fabricating oriented MOF membranes is a top–down approach involving the synthesis or exfoliation of H_2-selective MOF nanosheets. Zhang *et al.* reported a 2D Co-based MOF nanosheet hollow fiber membrane through a vapor phase transformation strategy.[68] A 57-nm-thick $Co_2(bim)_4$ film was transformed from the Co-based gel layer via ligand vapor phase transformation. The gel layer has a multifunctional role such as providing an active metal source, guiding the oriented growth of the nanosheets, and controlling the membrane thickness in the formation of the nanosheet membrane. The resulting $Co_2(bim)_4$ film exhibited separation performance with H_2/CO_2 selectivity of 42.7 and H_2 permeance of 507 GPU. Yang *et al.* introduced a novel method for ultrathin MOF films utilizing lamellar $Zn_2(bim)_4$ nanosheets as building blocks.[59] Initially, they exfoliated $Zn_2(bim)_4$ nanosheets from a bulk cubic powder by means of wet ball milling and ultrasonication. Subsequently, they fabricated a MOF film that was 10-nm-thick by hot drop-casting the nanosheet dispersion onto a 120 °C Al_2O_3 substrate [Figs. 17(a)–17(c)]. The MOF membrane, with a transmembrane pressure difference of 0 bar, exhibited a H_2/CO_2 selectivity of 291 and a H_2 permeance of 2700 GPU. To further expand on this concept, the researchers synthesized another 2D nanosheet of $Zn_2(bim)_3$ using a top–down exfoliation method.[87] The $Zn_2(bim)_3$ nanosheets were only 1.6 nm thick. A10-nm-thick

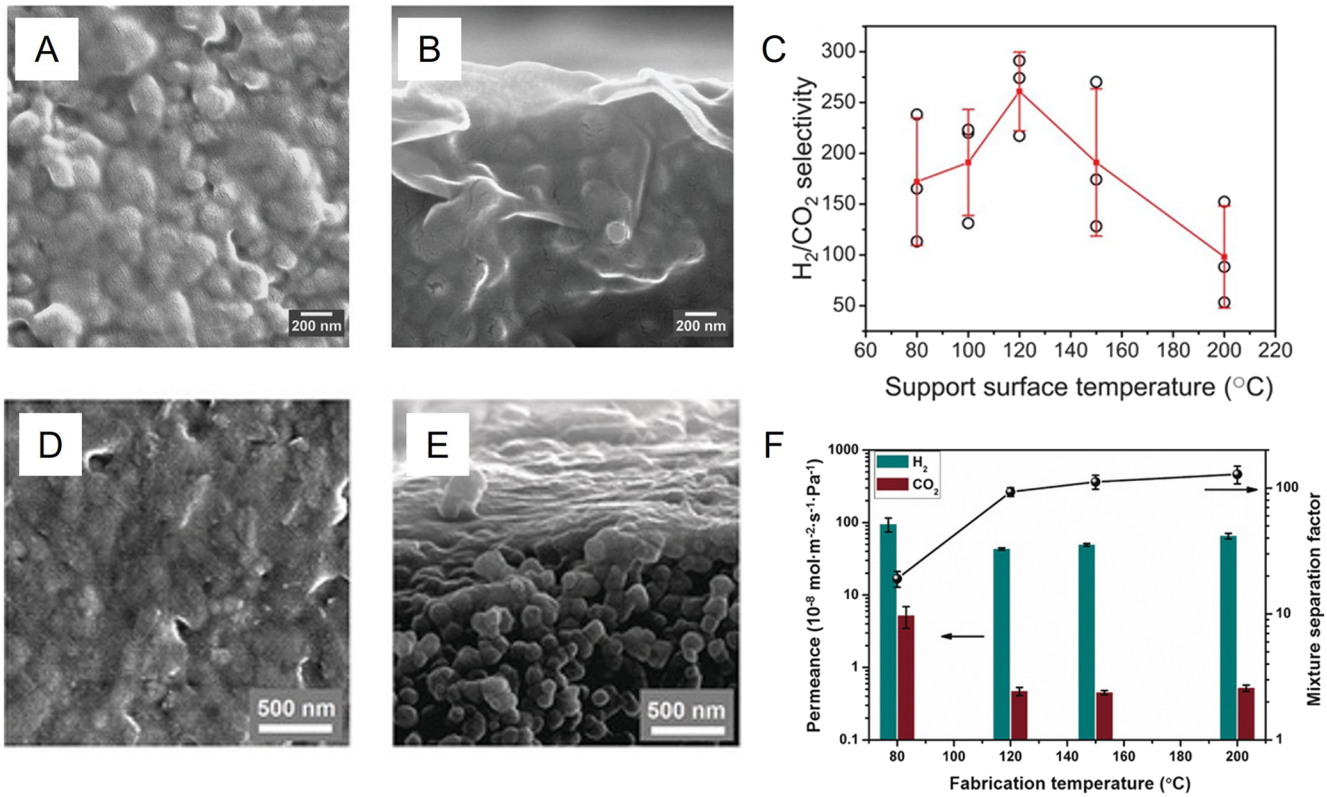

FIG. 17. (a) SEM top view and (b) cross-sectional view of a $Zn_2(bim)_4$ nanosheet layer on α-Al_2O_3 support. (c) Scatter plot of H_2/CO_2 selectivities measured from 15 membranes. The red line with symbols shows the average selectivity and dispersion of selectivity of the membranes prepared at different coating temperatures.[87] Reprinted with permission from Peng *et al.*, Angew. Chem., Int. Ed. **56**(33), 9757–9761 (2017). Copyright 2017 from Wiley. (d) SEM images of the top view and (e) cross-section view (bottom right) of the $Zn_2(bim)_3$ nanosheet membranes); (f) binary gas separation performance of equimolar H_2/CO_2 through the $Zn_2(bim)_3$ nanosheet membranes prepared at different temperatures via the hot-drop coating method.[59] Reprinted with permission from Peng *et al.*, Science **346**(6215), 1356–1359 (2014). Copyright 2014 from AAAS.

stacked film demonstrated a hydrogen permeance of 3136 GPU and H_2/CO_2 selectivity of 130 [Figs. 17(d)–17(f)]. Zhao *et al.* utilized a mild freeze-thaw approach to exfoliate MAMS-1 crystals and produce 12–40 nm films of 2D MAMS-1 nanosheets on AAO.[118] Of these films, the 40-nm-thick film exhibited the best overall performance, with an H_2 permeance of 800 GPU and an H_2/CO_2 selectivity of 268. The MAMS-1 showed a pore opening phenomenon between −196 and 20 °C, with increasing temperature causing an intensified vibrational mode of the tert-butyl groups, leading to a lattice expansion in the *ab* plane. However, above 60 °C, the H_2 permeance decreased, and the film became nearly impermeable at 100 °C. This decrease in permeance was attributed to the reduction in interlayer distance in the c direction upon heating. XRD analysis at temperatures ranging from 20 to 100 °C indicated a shift in the (002) crystal plane, reflecting a contraction of the lattice spacing from 1.90 to 1.79 nm. As a result of this contraction, the rotation of the tert-butyl groups was significantly sterically hindered, leading to a decrease in permeance.

Overall, several pure MOF membranes have demonstrated exceptional H_2/CO_2 separation performance. However, these membranes still encounter challenges related to pressure stability arising from grain boundary effects and linker rotation. Consequently, the application of MOF membranes in high-pressure operations remains unexplored. Addressing this issue will be crucial for realizing practical applications of MOF membranes in H_2/CO_2 separations.

3. C_3H_6/C_3H_8 separation

Separating olefins from paraffins is a crucial process in the chemical industry, but the traditional method of cryogenic fractional distillation is highly energy-intensive.[58,114] Membrane technology presents a promising alternative for olefin/paraffin separations as it eliminates the necessity for phase change. However, this separation remains challenging because of their similar kinetic diameters [$d(C_3H_6)$ = 4.0 Å and $d(C_3H_8)$ = 4.3 Å].[114] To achieve this, a rough estimate of the desired membrane performance would be to achieve a C_3H_6/C_3H_8 selectivity greater than 35[119,120] and C_3H_6 permeance of the order of 100 GPU. Among the membrane materials, MOF films have shown potential for C_3H_6/C_3H_8 separation due to their rigid structure, which endows the film with a strong molecular sieving performance.

Table IV presents the selectivity and permeance data for the most effective ultrathin MOF films for separating C_3H_6/C_3H_8, as

TABLE IV. Summary of thin MOF membranes for C_3H_6/C_3H_8 separation.

MOF	Highlight	Thickness (nm)	T (°C)	Pressure (atm)	Gas pair	Permeance (GPU)	Separation factor	Reference
ZIF-8	ENACT approach	360	25	1	C_3H_6/C_3H_8	40	33	63
ZIF-8	ZIF-8_Cm phase dominated	205	25	1	C_3H_6/C_3H_8	54	300	60
ZIF-8	Low current density ACD approach in fully aqueous phase	500	25	1	C_3H_6/C_3H_8	182	142	64
Zr-fum-fcu-MOF	High pressure resistance due to the linker rigidity	150	25	7	C_3H_6/C_3H_8	120	125	85
ZIF-8	IOR strategy for thin MOF film	180	25	1	C_3H_6/C_3H_8	386	120	108
ZIF-8	Full vapor treatment	100	25	7	C_3H_6/C_3H_8	70	300	58
ZIF-8	Gel-vapor deposition	~17	25	1	C_3H_6/C_3H_8	170	70.8	55
DZIF-8	Defective ZIF-8	45–150	25	1	C_3H_6/C_3H_8	2000–3000	90–120	70

reported in the literature. These reports indicate that the separation of C_3H_6/C_3H_8 has mainly been limited to ZIF-8. However, a few other MOF membranes, such as those made of fcu-MOFs, also exhibit attractive C_3H_6/C_3H_8 separation performance.

The electro-chemical deposition method offers a controllable approach to synthesize defect-free ZIF-8 membranes, enabling efficient C_3H_6/C_3H_8 separations. Our group reported a novel method to fabricate defect-free MOF films, which we called "electrophoretic nuclei assembly for crystallization of highly intergrown thin-films" (ENACT).[63] Thin nuclei film (~100 nm thick) could be prepared by electrophoretic deposition of a few nanometer sized nuclei spontaneously forming in the growth solution. Following this, a 360-nm-thick ZIF-8 membrane was synthesized on AAO substrates, which yielded a C_3H_6/C_3H_8 selectivity of 33 and a C_3H_6 permeance of 40 GPU. Wang *et al.* extended the application of electrochemical synthesis of MOF films by using a fast current-driven synthesis method.[60] They successfully synthesized 200-nm-thick ZIF-8 films composed of a novel polymorph of ZIF-8_Cm. The researchers discovered that the ZIF-8_Cm polymorph exhibited less flexibility in terms of linker rotation when compared to the more common ZIF-8_I43m polymorph. Moreover, the new polymorph demonstrated exceptional separation performance, with a C_3H_6 permeance of 52 GPU and a C_3H_6/C_3H_8 selectivity of 304. This separation performance was attributed to the beneficial lattice distortion caused by the electric field applied during synthesis. Lai *et al.* reported the successful synthesis of the ZIF-8 membrane via the ACD approach.[64] The 500 nm thick defect-free ZIF-8 membrane was deposited on AAO substrates in a fully aqueous phase under an extremely low current density (0.13 mA cm^{-2}) within 60 min. The resulting ZIF-8 membrane exhibited exceptional separation performance, with a C_3H_6 permeance of 182 GPU and a C_3H_6/C_3H_8 selectivity of 142. Wang *et al.* employed an inhibited Ostwald ripening (IOR) technique to produce ultrathin ZIF-8 films using electrochemical synthesis.[108] They incorporated the polymer-based inhibitors to restrain the metal-organic coordination for ZIF-8, resulting in a decrease in the film thickness. The produced membranes were 180-nm-thick and demonstrated a high C_3H_6/C_3H_8 separation performance, with the C_3H_6 permeance of 386 GPU and the C_3H_6/C_3H_8 separation factor of 120.

In addition to ZIF-8, applying the electro-chemical deposition method to other pressure-stable MOF membranes can enhance their pressure stability as well. Recently, Eddaoudi *et al.* reported the electrochemical synthesis of a series of defect-free fcu-MOF polycrystalline membranes with molecular sieving abilities for hydrocarbon separations. A 150-nm-thick Zr-fum-fcu-MOF film displayed a C_3H_6 permeance of 120 GPU and a C_3H_6/C_3H_8 selectivity of 125.[85] Furthermore, these membranes displayed excellent pressure-resistant capability and demonstrated an increased separation factor for C_3H_6/C_3H_8 mixtures at practical feed pressures of up to 7 atm. This increase was due to the triangular pore apertures in Zr-fum-fcu-MOF that are constrained by fumarates with non-rotating C=C double bonds, which provided the necessary intrinsic rigidity to prevent deformation under high pressures, thereby preserving the molecular sieving ability.

Apart from electrochemistry, various other deposition methods can also be employed for the growth of MOF membranes. Zhang *et al.* utilized a gel-vapor deposition technique for creating ultrathin ZIF-8 films, measuring ~17 nm.[55] This method involves a combination of sol-gel coating and 2-methylimidazole vapor deposition, which allows for the transformation to ZIF-8 without the use of solvents. Due to the film thinness, they displayed a C_3H_6 permeance of 170 GPU with a C_3H_6/C_3H_8 selectivity of 70.8. Tsapatsis *et al.* developed a novel all-vapor technique for fabricating a 100-nm-thick defect-free ZIF-8 thin film on a ZnO-modified α-alumina support called ligand-induced permselectivation.[58] The resulting ZIF-8 membranes demonstrated excellent performance, with a C_3H_6/C_3H_8 selectivity of 110 and a C_3H_6 permeance of 152 GPU. The procedure involves modifying the porous support with ZnO until it becomes impermeable, indicating that the substrate has been sufficiently coated with dense ZnO. ZIF-8 was then formed within the porous support by vaporizing 2-methylimidazole in the presence of the modified substrate.

Defect-engineered MOFs hold great potential to significantly elevate the separation performance by enhancing the interactions between propene molecules and the open metal sites. Zhong *et al.* developed one of the thinnest ZIF-8 membranes to date, which is supported on commercial ultrafiltration polysulfone (PSf) porous substrates using interface layer polarization induction.[70] The

resulting defective ZIF-8 (DZIF-8) membranes had a thickness of only ~45 nm and exhibited exceptional propylene permeance of 2000–3000 GPU and a remarkable propylene/propane separation factor of 90–120. This high separation factor is believed to be due to the presence of abundant open metal sites capable of forming π bond interactions with propylene molecules.

Overall, numerous ultrathin MOF membranes, particularly from the ZIF-8 framework, have been utilized for efficient C_3H_6/C_3H_8 separation through various deposition and growth methods. The tunable and highly selective pore structure of ZIF-8 enables preferential adsorption of propylene over propane, benefiting from the size disparity between the two molecules. Ongoing research has explored different strategies to enhance pressure stability while maintaining exceptional separation performance. The remarkable chemical and thermal stability further solidify its potential for practical applications in gas separation processes, positioning it as a promising candidate for industrially significant propylene and propane separations.

B. Ultrathin MOF films in selective ion separation application

The separation of protons and ions is important for fundamental as well as technological advancements, with the latter ranging from water purification to energy storage. MOF films have emerged as a promising solution for this, thanks to their distinct porous structure and functionality. The design of continuous thin films makes them an ideal candidate for integration into devices such as proton exchange membrane fuel cells (PEMFCs), where effective proton transport is crucial, and in desalination processes, which demand the selective removal of certain ions.

The performance of PEMFCs relies heavily on proton conductance within the PEM. The proton movement is primarily facilitated by two mechanisms, the Grotthuss mechanism[121] and the vehicle mechanism.[122,123] The Grotthuss mechanism, commonly referred to as "proton hopping," involves the proton relayed along a sequence of hydrogen-bonded water molecules and hydronium ions. While the vehicle mechanism involves the migration of hydronium ions through the membrane, proton transport based on the Grotthuss mechanism is more efficient as it is less affected by the surrounding medium.

Ion–ion separation in membranes is influenced by a combination of factors: size exclusion, charge exclusion (Donnan exclusion), dielectric effects, and van der Waals forces.[124] A few small pore MOF structures offer size-based selectivity, with pores that allow ions of certain dimensions to pass while blocking larger ones. Donnan exclusion from MOFs with charged surfaces also plays a role, causing ions with a similar charge (positive or negative) as that of the pore to be excluded from the pore. In several cases, pores can force the ions to undergo partial dehydration. The energy barriers created by these combined effects are critical in determining the efficiency of ion separation.

1. Proton conduction

Proton exchange membrane fuel cells (PEMFCs) are seen as one of the potential solutions to renewable energy storage, thanks to their low operating temperature compared to other fuel cells such as those based on solid oxide, high energy density, and low carbon emissions.[125–127] PEMFCs typically operate within the range of 60–85 °C for low-temperature systems and 120–140 °C for high-temperature systems. Their performance can be improved by strategies that promote proton migration. One of these includes the use of ultrathin MOF films as PEM. To facilitate high proton conductivity, various ligands with functional groups ($-SO_3H$, $-NH_2$, –COOH, imidazole, ammonium cations, etc.) have been used.[128–130] While several MOFs have proton conductance levels comparable to Nafion, a widely used commercial PEM material with a conductance of 0.05–0.20 S cm^{-1} at room temperature, most studies have only been conducted in pellet form, with only a few in thin film morphology.

Deoxyribonucleic acid (DNA)-encapsulated ZIF-8 membranes exhibited proton conductivity of 3.40×10^{-4} S cm^{-1} at 25 °C and 0.17 S cm^{-1} at 75 °C.[131] These membranes also demonstrated a low methanol permeability of 1.25×10^{-8} cm^2 s^{-1}, effectively inhibiting methanol migration from anode to cathode, which might degrade the cell performance in the methanol-based fuel cell. This combination of properties enhances the practical applicability of these membranes in PEM fuel cells. These membranes were prepared by a composite of zinc hydroxide nanostrands and single-strand DNA, which were then immersed in HmIm. The advantage of this approach is that single-strand DNA builds hydrogen bond networks with water molecules and facilitates proton migration. Another study utilized sulfonated spiropyran (SSP)-encapsulated ZIF-8 membranes to demonstrate a light-responsive, on/off proton conductivity ratio of 2.8×10^4. This was attributed to the photoactive SSP, where hydrophilic group density could be altered by the conversion of SSP between merocyanine and spiropyran forms.[132] The membranes exhibited a proton conductivity of 0.043 S cm^{-1} at 75 °C.

In another approach, hourglass-shaped nanochannels (NC) of polyethylene terephthalate (PET) were utilized to grow MIL-121, MIL-53(Al), and MIL-53(Al)–NH_2 MOF crystals. The experiment was designed to grow MOF crystals in the PET nanochannel via counter-diffusion.[133] Unidirectional proton conduction was observed from polymer to MOF. A strong rectification of up to 500 was reported and was attributed to a low energy barrier in proton transport from disordered water clusters in PET nanochannels to ordered water clusters in MOF. Proton conductivities of 240, 145, and 70 mS cm^{-1} were reported for MIL-121, MIL-53, and MIL-53-NH_2, respectively. This was in agreement with the number of hydrogen-bonded pathways for proton transport in these MOFs, as revealed by a dedicated molecular dynamics simulation.

Overall, polycrystalline MOF membranes have exhibited attractive proton conductivity for PEM applications, as summarized in Table V. However, these membranes still face significant challenges with regard to their structural stability and rigidity, and, as such, the applications of MOF membranes in practical PEMFC have not been extensively explored. High performance, stable, and defect-free MOF membranes with high proton conductivity and high gas barrier properties will be required in the practical applications of PEMFC.

2. Ion–ion separation

The development of ion-selective channels has shown great potential in alkali metal extraction, molecular separation, and biosensing. MOFs have emerged as promising materials for ion–ion separation due to their unique pore size, which falls between the

TABLE V. Summary of thin MOF membranes for proton conductance.

MOF	Fabrication method	Thickness	Proton conductivity	Reference
DNA@ZIF-8	Solid confinement conversion	500 ± 50 nm	3.4×10^{-4} S cm^{-1} at 25 °C under 97% RH 0.17 S cm^{-1} at 75 °C under 97% RH	131
SSP@ZIF-8	Solid confinement conversion	~500 nm	1.7×10^{-4} S cm^{-1} at 25 °C under 95% RH 0.043 S cm^{-1} at 75 °C under 95% RH	132
MIL-53 (Al) MIL-53 (Al)–NH_2 MIL-121	Counter-diffusion growth	Hourglass-shaped nanochannel[a]	~0.145 S cm^{-1} ~0.07 S cm^{-1} ~0.24 S cm^{-1}	133

[a]Hourglass-shaped nanochannel: large base diameter~530 nm; small base diameter~140 nm; tip diameter~18 nm; length: 12 μm.

diameters of partially dehydrated and hydrated ions. In addition, the presence of open metal sites and charges in MOF ligands is attractive for charge-based (Donnan exclusion) ion transport.[134–136] Current-voltage (I–V) by ion drift measurements[86,137,138] as well as electrodialysis[139,140] have been extensively used to study MOF membranes for ion separation.

The ion separation performance of several MOF membranes has been investigated. For instance, the SSP@ZIF-8 membrane has shown ideal selectivity of 77, 112, and 4913 for Li^+ over Na^+, K^+, and Mg^{2+}, respectively.[141] This selectivity was attributed to the much smaller size of dehydrated Li^+ ions driven by an external electric field. UiO-66-NH_2 and UiO-66-SO_3 membranes, fabricated using *in situ* growth on the AAO substrates held in the diffusion cell, demonstrated excellent saline water stability.[139,140] The UiO-66-NH_2 membrane exhibited high selectivity for monovalent ions (Na^+ and Li^+) over bivalent ions (Mg^{2+}), with selectivities of ~200 and ~60, respectively. This was attributed to the intrinsically uniform pore size of the UiO-66-NH_2 framework, which is lower than the hydration diameter of Mg^{2+}.[139] On the other hand, the UiO-66-SO_3H membrane yielded a higher cation permeation compared to that from the UiO-66-NH_2 membrane. This was attributed to the facilitation of cation permeation by the SO_3H functional groups compared to the –NH_2 groups.[140] Another study using counter-diffusion synthesis of the ZIF-8 membrane using graphene oxide nanosheets reported a Li^+/Rb^+ selectivity of 4.6.[137] This was attributed to a strong interaction between water molecules and ZIF-8 frameworks, resulting in partial dehydration of the ions in ZIF-8. In this case, partial dehydration imparted higher Li^+ mobility in ZIF-8.

Recent studies have investigated the use of UiO-66 crystals filled into bullet-shaped poly(ethylene terephthalate) nanochannels (PET-NC)[142] to achieve high ion–ion selectivity among various cations[137,138,143–146] and anions.[147] These nanochannels have a tip diameter of ~30–50 nm, a base diameter of ~300–500 nm, and a length of 12 μm. PET-NC allows for preferential ion current direction from tip to base due to the deprotonated carboxylic groups on the channel wall, leading to fast metal ion transport.[138,148] Studies examining UiO-66-X [X = H, NH_2, and $N^+(CH_3)_3$] PET-NC have demonstrated F^-/Cl^- selectivity of 53, 83, and 192, respectively. This was attributed to a decreased pore size and a preferential binding of F^- with the open metal sites on the UiO-66.[147] Sulfonated UiO-66-X [X = SAG, NH-SAG, $(NH\text{-}SAG)_2$ where SAG refers to sulfonic acid] PET-NC channels yielded high proton selectivity over other cations (K^+, Na^+, and Li^+) due to the formation of proton channels from a high density of sulfonic acid groups.[143] UiO-66-$(NH\text{-}SAG)_2$ PET-NC exhibited the highest proton selectivity among the three UiO-66-X channels, with H^+/Li^+, H^+/Na^+, and H^+/K^+ of ~100, 80, and 70, respectively. UiO-66-COOH and UiO-66-NH_2 were synthesized in ethanediamine (EDA)-functionalized PET-NC to evaluate the effect of the surface charge.[145] The negatively charged UiO-66-COOH-NC showed about two orders higher K^+/Mg^{2+}, Na^+/Mg^{2+}, and Li^+/Mg^{2+} selectivity of 772, 563, and 137, respectively, than the selectivity of positively charged UiO-66-NH_2-NC. This was because UiO-66-COOH-NC exhibited a relatively low energy barrier (0.22 eV) for K^+ transport. Additionally, the effect of surface chemistry of PET-NC was systematically discussed by varying the functional group [ethylenediamine (EDA) and (3-aminopropyl)triethoxysilane (APTMS)], shape {cylindrical, bullet, cigar, and hourglass [Fig. 18(a)]}, size, and density of nanochannels.[146] UiO-66-$(COOH)_2$ synthesized in cylindrical EDA-functionalized PET-NC channels displayed the highest Li^+/Mg^+ selectivity of 3077, while a multichannel with a pore density of 10^6/cm^2 yielded a Li^+/Mg^{2+} selectivity of 50.

Asymmetric UiO-66-$(COOH)_2$ PET-NC was reported by the counter-diffusion growth [Fig. 18(b)], which enabled a higher rectification ratio due to the higher concentration of negative charges in the tip region compared to the fully filled PET-NC.[138] The resulting UiO-66-$(COOH)_2$ PET-NC showed ultrahigh K^+/Mg^{2+}, Na^+/Mg^{2+}, and Li^+/Mg^{2+} of 4948, 3230, and 1590 [Figs. 18(c) and 18(d)], respectively. This was because of the interaction between ions and carboxyl groups, which then reduces the energy barrier for monovalent cations across the nanochannel. 4′-aminobenzo-15-crown-5 ether (15C5)-modified UiO-66-$(COOH)_2$ PET-NC yielded a high Na^+ selectivity over K^+ and Li^+ of 360.1 and 1770, respectively, comparable to the biological systems.[144] In addition, a rectifying effect has been observed due to the asymmetric modification of 15C5 on the sides of the nanochannel. These results demonstrate the potential of MOF membranes for efficient ion–ion separation in various applications.

MOF membranes with high ion–ion separation performance are summarized in Table VI. While some membranes/nanochannels have shown promising results for separating mono/divalent ions through different testing methods, it is important to acknowledge

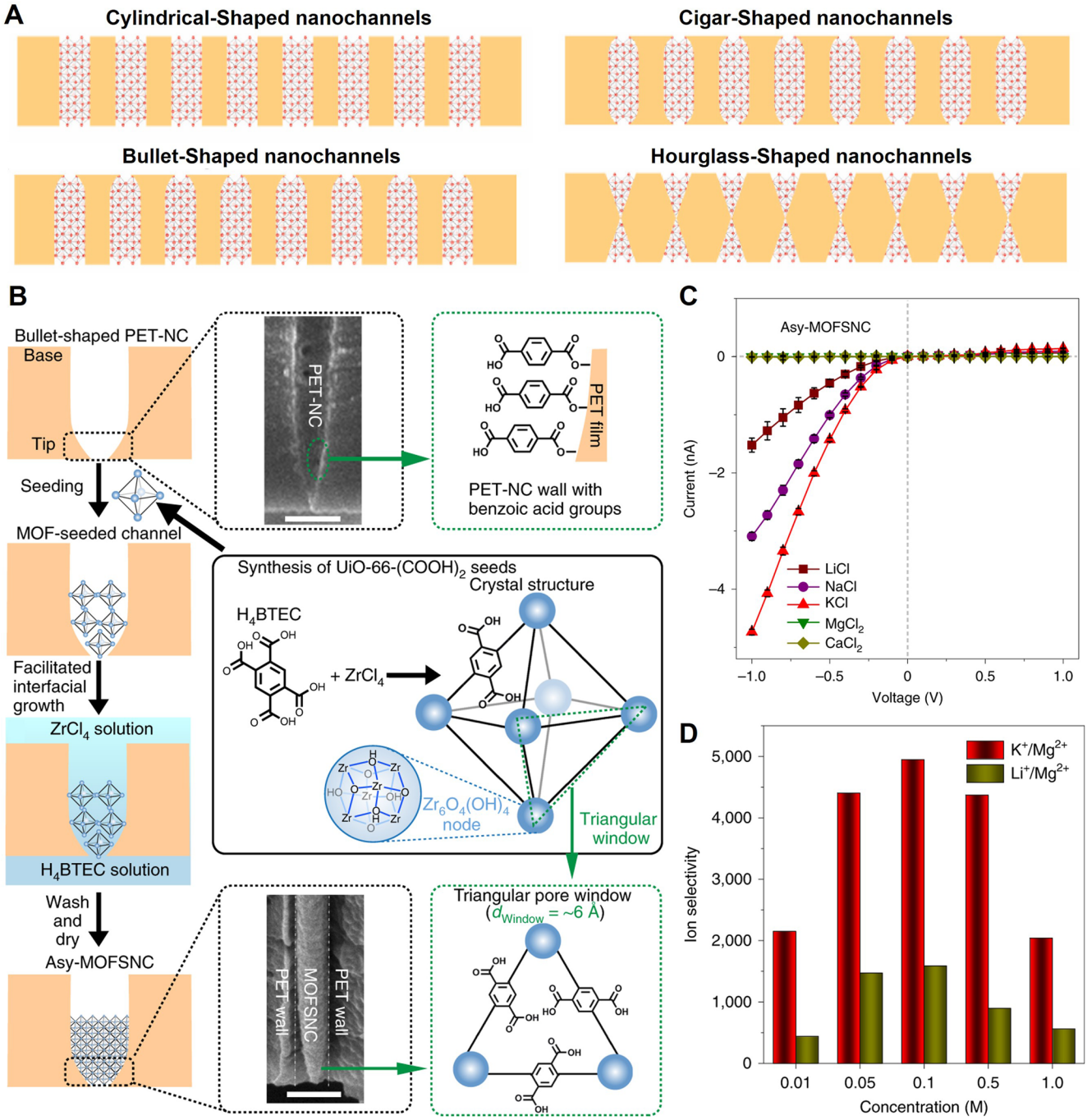

FIG. 18. (a) Scheme of PET-NCs with different channel shapes.[146] Reprinted with permission from Hou *et al.*, J. Membr. Sci. **674**, 8 (2023). Copyright 2023 Elsevier. (b) Scheme and SEM images of the fabrication of asymmetric UiO-66-$(COOH)_2$ PET-NC. (c) I–V curves of asymmetric UiO-66-$(COOH)_2$ PET-NC measured in 0.1M electrolyte solutions. (d) Ion selectivities of UiO-66-$(COOH)_2$ PET-NC at different ion concentrations.[138] Reprinted with permission from Lu *et al.*, Nat. Mater. **19**(7), 767 (2020). Copyright 2020 Springer Nature.

TABLE VI. Summary of thin MOF membranes and nanochannels for ion separation.

MOF	Fabrication method	Thickness	Ion selectivity	Reference
SSP@ZIF-8	Solid confinement conversion	~500 nm	$Li^+/Na^+ = 77$ $Li^+/K^+ = 112$ $Li^+/Mg^{2+} = 4913$	141
UiO-66-NH_2	*In-situ* growth	<500 nm	$Na^+/Mg^{2+} \sim 200$ $Li^+/Mg^{2+} \sim 60$	139
UiO-66-SO_3H	*In-situ* growth	<600 nm	$K^+/Mg^{2+} = 5091$ (ideal); 5.31 (binary) $Na^+/Mg^{2+} = 2449$ (ideal); 170 (binary) $Li^+/Mg^{2+} = 776$ (ideal); 1.88 (binary)	140
ZIF-8	Counter-diffusion growth	446 ± 74 nm	LiCl/RbCl ~ 4.6	137
UiO-66-$(NH\text{-}SAG)_2$	*In-situ* growth	Bullet-shaped nanochannel[a]	$H^+/Li^+ \sim 100$ $H^+/Na^+ \sim 80$, $H^+/K^+ \sim 70$	143
UiO-66	*In-situ* growth	Bullet-shaped nanochannel[a]	LiCl/RbCl ~ 1.8	137
UiO-66-$(COOH)_2$	Counter-diffusion growth	Bullet-shaped nanochannel[a]	$K^+/Mg^{2+} = 4948$ $Na^+/Mg^{2+} = 3230$ $Li^+/Mg^{2+} = 1590$	138
UiO-66-COOH UiO-66-NH_2	*In-situ* growth	Bullet-shaped nanochannel[a]	$K^+/Mg^{2+} = 772.6$ $Na^+/Mg^{2+} = 563.0$ $Li^+/Mg^{2+} = 136.5$ $K^+/Mg^{2+} = 5.7$ $Na^+/Mg^{2+} = 4.6$ $Li^+/Mg^{2+} = 1.3$	145
15C5-UiO-66-$(COOH)_2$	Counter-diffusion growth	Bullet-shaped nanochannel[a]	$Na^+/K^+ = 360.1$ $Na^+/Li^+ = 1770$	144
UiO-66 UiO-66-NH_2 UiO-66-$N^+(CH_3)_3$	*In-situ* growth	Bullet-shaped nanochannel[a]	$F^-/Cl^- \sim 53.08$ $F^-/Cl^- \sim 83.16$ $F^-/Cl^- \sim 192.04$	147

[a]Bullet-shaped nanochannel: tip diameter ~30 to 50 nm; base diameter ~300 to 500 nm; length: 12 μm.

that comparing ion–ion selectivity across different measurements is not straightforward as the underlying ion transport mechanisms vary significantly. Moving forward, the development of MOF membranes for ion–ion separation should be innovated considering real-world situations; for instance, exploring the potential of these membranes in energy storage devices including redox flow batteries and fuel cells and in lithium mining through techniques such as electrodialysis or nanofiltration.

3. Desalination

Freshwater scarcity is anticipated to be one of the most significant challenges that humanity will face in the forthcoming decades. A vast yet underutilized resource for addressing this issue is saline water, where drinking water can be obtained by the desalination process, which removes ions and minerals from saline water. Membrane separation technology has been highly successful in this process, saving significantly more energy (>90%) compared to the conventional distillation process.[109] Membrane-based desalination is currently commercialized on a large scale, where membranes are made of polyamide selective layers. MOFs are emerging as promising materials for water desalination due to their unique properties. MOFs are characterized by their high porosity and tunable pore size, which can lead to high water permeance and excellent salt rejection rates. Certain MOFs such as UiO-66 exhibit excellent chemical stability, enabling them to withstand the harsh treatment conditions often encountered in desalination processes.

Research on MOF-based membranes for desalination has been dominated by nanocomposites of MOF particles and polymers (so-called mixed-matrix membranes), and polycrystalline MOF films for water purification have not been intensively studied.[61,149–151] In the following paragraph, we present some examples of ultrathin polycrystalline MOF films that demonstrate efficient desalination.

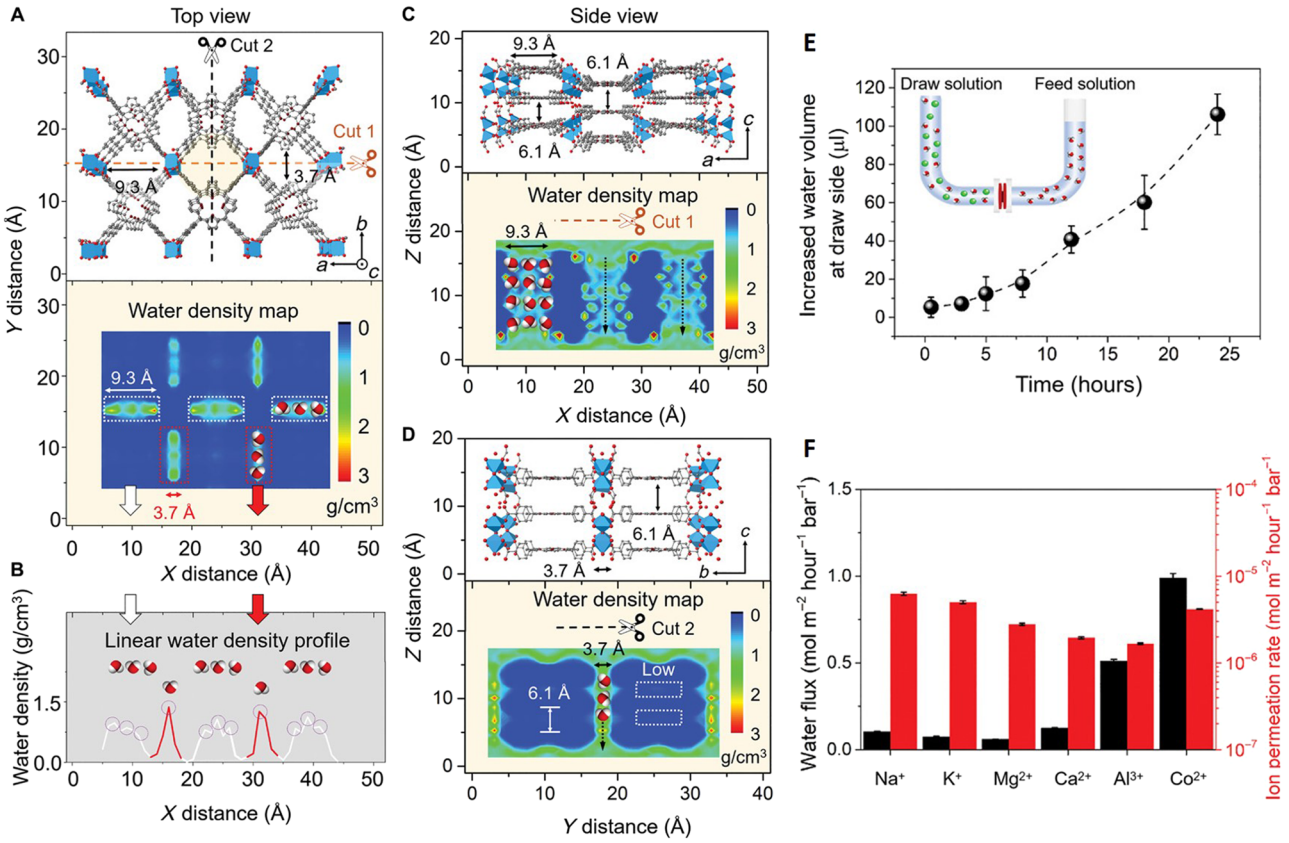

FIG. 19. (a)–(d) Molecular dynamics model illustrating the distribution of water molecules within the Al-MOF nanosheet membrane under AB stacks. (a) Top view of the water density map. (b) Corresponding linear gradient profile derived from the top view. (c) and (d) Side views of the water density map along two different sections: cut 1 and cut 2, respectively. (e) Plot depicting the increase in volume over time during the diffusion process. (f) Water flux measurements obtained using different salt solutions.[57] Reprinted with permission from Jian *et al.*, Sci. Adv. **6**(23), eaay3998 (2020). Copyright 2020 AAAS.

TABLE VII. Summary of thin MOF membranes for desalination.

MOF	Fabrication method	Thickness (nm)	Water permeance and salt rejection	Reference
Al-MOF	Vacuum filtration	100	0.0396 l m^{-2} h^{-1} bar^{-1} NaCl, KCl, $MgCl_2$, $CaCl_2$, $AlCl_3$, and $CoCl_2$ ~ 100%	57
ZIF-8/TA	*In-situ* growth	50	3.6 l m^{-2} h^{-1} bar^{-1} NaCl: 64.7%; Na_2SO_4: 92.2%	152
ZIF-8/(TA-Zn^{2+})$_2$	Layer-by-layer	85	5.1 l m^{-2} h^{-1} bar^{-1} NaCl: 55.2%; Na_2SO_4: 93.6%	100
ML-UiO-66	*In-situ* growth	103 ± 14	~29.8 l m^{-2} h^{-1} NaCl: 99.99%	89
UiO-66	*In-situ* growth	120 ± 20	~19.9 l m^{-2} h^{-1} NaCl: 99.99%	89

One promising report of an ultrathin MOF membrane is based on aluminum tetra-(4-carboxyphenyl) porphyrin framework MOF (Al-MOF).[57] The membrane was prepared by the filtration of Al-MOF nanosheets. The aligned pore channels of Al-MOF nanosheet film [Figs. 19(a)–19(d)] facilitated water flow while preventing the diffusion of ions, leading to >99.99% salt rejection and a water flux of 2.2 mol m^{-2} h^{-1} bar^{-1} [Figs. 19(e) and 19(f)]. In another study, ZIF-8 membranes were developed by coating tannic acid (TA) on PES substrates. ZIF-8/TA and ZIF-8/(TA-Zn^{2+}) membranes were fabricated through *in situ* growth of the ZIF-8 precursor and the layer-by-layer (LBL) method by immersing the TA-coated substrate in zinc acetate and 2-methylimidazole separately, respectively.[100,152] Both membranes exhibited high water permeance and NaCl and Na_2SO_4 rejection. We do note that ZIF-8 stability in an aqueous environment is arguable. There are many studies that show the rapid dissolution of ZIF-8 in water.[153–155]

UiO-66 and missing-linker UiO-66 (ML-UiO-66) membranes showed ultrahigh water flux of 19.9 and 29.8 l m^{-2} h^{-1}, respectively, with NaCl rejection of 99.99%.[89] The superior performance of these membranes can be attributed to the size sieving effect of the rigid pore, which allows the realization of very high rejection. In addition, the missing linker defect increases hydrophilicity, facilitating water transport.

Despite the promising performance of MOF membranes in water desalination (Table VII), their practical implementation in the industry is hindered by significant challenges including scalability and high cost. Additionally, the production of defect-free MOF membranes on an industrial scale remains a major hurdle to their widespread adoption. As a result, despite their potential utility, MOF membranes are still in the early stages of development and are far from being ready for commercial use in water desalination.

IV. PERSPECTIVE

Overall, ultrathin MOF films from several different frameworks have been demonstrated using various crystallization and fabrication strategies. Several of these films have demonstrated exceptional performance in gas and ion separations, making them highly attractive for membrane-based separation applications. However, the field is still far from its true potential. Concerning membrane morphology, an important question to pose is whether the thickness of MOF films can be reduced down to the thickness limit, i.e., to unit-cell thickness.[156] This will require further fine-tuning of the crystallization conditions that promote in-plane growth of the film but completely suppress out-of-plane growth. Successful realization of this feat will bring MOF membranes into the class of other 2D films such as graphene, where MOFs will have a big advantage, i.e., uniform and high density of pores in MOF.

From a structure–property relationship point of view, while there is agreement that thinner MOF films lead to higher permeance, there are several other important aspects that control molecular permeance. This includes support resistance, lattice flexibility, the use of functional groups that may enhance the adsorption of a component and improve its uptake at a lower concentration, and measurement techniques.

When designing ultrathin MOF film, one must consider the support permeance. Traditional inorganic supports such as those prepared using asymmetric ceramic layers may or may not match the permeance of the MOF film. If their permeance does not match that of the MOF film, then the overall permeance as well as the molecular selectivity are restricted by the support. This can be determined by a simple calculation using the transport resistance model, taking support and MOF film resistance in series.

A large variation in the performance of MOF membranes across the literature, especially for bidentate MOFs with flexible lattice, can be attributed to the strain in the film, which controls lattice flexibility and, hence, molecular permeance and selectivity. This is especially true for ultrathin films, where a selective layer could often be confined near support pores, generating strain in the lattice. Currently, there is no systematic data on the effect of lattice strain in various support configurations or the effect of film thickness on the gas pair selectivity. Such analyses will be extremely useful for the field because several important separations from MOF membranes (e.g., C_3H_6/C_3H_8 from ZIF-8) rely on the kinetic diffusion of gases through a flexible lattice. Therefore, methods that control and tune lattice flexibility will be extremely useful in tuning gas pair selectivity as well as gas permeance. Some progress has been made in this respect, e.g., rapid heat treatment,[113] current-driven synthesis,[56,60,64,85] etc. An additional advance is needed to improve the separation performance in a region of commercial interest.

Reports that facilitate the adsorption of molecules on MOFs, e.g., by functionalization or by improving electrostatic interaction, hydrogen bonding, van der Waals and $\pi\cdots\pi$ interaction, etc., have started to emerge. Such approaches are highly attractive because they improve the performance of membranes. However, careful consideration should be given to performance as a function of molecular activity, especially in gas mixtures, as well as poisoning of the functional group, e.g., by trace amounts of impurities. Finally, while several studies report high performance using isobaric measurements where the net pressure difference between the feed side and the permeate side is close to zero, often the performance drops upon pressurization of the film. Therefore, one should carefully assess the role of pinhole defects in the film and accompanying nonselective viscous transport as opposed to selective diffusion from MOF pores. A combination of molecular-sieving and competitive interactions will likely yield the best-performing membranes.

Last but not least, the scalability of MOF membranes is always one of the most concerning aspects of meeting realistic conditions. This includes the use of low-cost supports, e.g., polymeric supports. These supports can be fabricated either as a flat sheet (~10 \$ m^{-2}) for spiral-wound modules or as hollow fibers (~2–5 \$ m^{-2}) for hollow-fiber modules.[14] There are already several pioneering examples in this respect, e.g., interfacial crystallization and gel vapor synthesis on polymer hollow fiber modules. Recently, the fabrication of MOF membranes on ceramic hollow fibers has been reported.[157] The development of a spiral-wound module would be attractive from the point of view that most reports have investigated the fabrication of MOF films on planar supports. Currently, spiral-wound modules based on ZIF-8 are being commercialized by UniSieve®, where the selective layer is trapped in the pores of the support, which helps to avoid crack formation in the film. Our view is that the availability of ultrathin MOF films down to a few nanometers in thickness may prevent crack formation tendency in MOF upon rolling the membrane element into a spiral-wound module.

ACKNOWLEDGMENTS

This research update is supported by the European Research Council Starting Grant (Grant No. 805437-UltimateMembranes), the Swiss National Science Foundation (SNSF) Assistant Professor Energy Grant (Grant No. PYAPP2_173645), and the SNSF project (Grant No. 20021_192005). Q.L. acknowledges funding by the Soochow University Starting Grant (Grant No. NH10902123).

AUTHOR DECLARATIONS

Conflict of Interest

The authors have no conflicts to disclose.

Author Contributions

Q.L., H.-Y.C., and S.S. contributed equally to this work.

Qi Liu: Conceptualization (equal); Data curation (equal); Formal analysis (equal); Investigation (equal); Methodology (equal); Validation (equal); Visualization (equal); Writing – original draft (equal); Writing – review & editing (equal). **Heng-Yu Chi**: Conceptualization (equal); Data curation (equal); Formal analysis (equal); Investigation (equal); Methodology (equal); Validation (equal); Visualization (equal); Writing – original draft (equal); Writing – review & editing (equal). **Shuqing Song**: Conceptualization (equal); Data curation (equal); Formal analysis (equal); Investigation (equal); Methodology (equal); Validation (equal); Visualization (equal); Writing – original draft (equal); Writing – review & editing (equal). **Ranadip Goswami**: Data curation (supporting); Formal analysis (supporting); Validation (supporting); Visualization (supporting); Writing – original draft (supporting); Writing – review & editing (supporting). **Kumar Varoon Agrawal**: Conceptualization (equal); Funding acquisition (lead); Project administration (lead); Resources (equal); Supervision (lead); Validation (equal); Visualization (equal); Writing – original draft (equal); Writing – review & editing (lead).

DATA AVAILABILITY

The data that support the findings of this study are available from the corresponding author upon reasonable request.

REFERENCES

[1] H. Furukawa, K. E. Cordova, M. O'Keeffe, and O. M. Yaghi, Science **341**(6149), 1230444 (2013).
[2] J.-R. Li, R. J. Kuppler, and H.-C. Zhou, Chem. Soc. Rev. **38**(5), 1477–1504 (2009).
[3] S. Qiu, M. Xue, and G. Zhu, Chem. Soc. Rev. **43**(16), 6116–6140 (2014).
[4] N. Stock and S. Biswas, Chem. Rev. **112**(2), 933–969 (2012).
[5] A. Schneemann, V. Bon, I. Schwedler, I. Senkovska, S. Kaskel, and R. A. Fischer, Chem. Soc. Rev. **43**(16), 6062–6096 (2014).
[6] Y. Bai, Y. Dou, L.-H. Xie, W. Rutledge, J.-R. Li, and H.-C. Zhou, Chem. Soc. Rev. **45**(8), 2327–2367 (2016).
[7] T. D. Bennett and A. K. Cheetham, Acc. Chem. Res. **47**(5), 1555–1562 (2014).
[8] N. Ma and S. Horike, Chem. Rev. **122**(3), 4163–4203 (2022).
[9] M. Kim, J. F. Cahill, H. Fei, K. A. Prather, and S. M. Cohen, J. Am. Chem. Soc. **134**(43), 18082–18088 (2012).
[10] L. M. Robeson, J. Membr. Sci. **320**(1–2), 390–400 (2008).
[11] L. M. Robeson, J. Membr. Sci. **62**(2), 165–185 (1991).
[12] H. B. Park, J. Kamcev, L. M. Robeson, M. Elimelech, and B. D. Freeman, Science **356**(6343), eaab0530 (2017).
[13] R. W. Baker and K. Lokhandwala, Ind. Eng. Chem. Res. **47**(7), 2109–2121 (2008).
[14] R. W. Baker, Ind. Eng. Chem. Res. **41**(6), 1393–1411 (2002).
[15] E. Ghasemiestahbanati, Y. H. Yoon, R. P. Lively, M. Shaibani, M. Majumder, and M. R. Hill, Carbon **203**, 856–864 (2023).
[16] Z. Liu, W. Qiu, W. Quan, and W. J. Koros, Nat. Mater. **22**(1), 109–116 (2023).
[17] L. Hu, K. Chen, W. I. Lee, K. Kisslinger, C. Rumsey, S. Fan, V. T. Bui, N. Esmaeili, T. Tran, and Y. Ding, Adv. Mater. **35**(26), 2301007 (2023).
[18] M. R. Rahimpour, F. Samimi, A. Babapoor, T. Tohidian, and S. Mohebi, Chem. Eng. Process.: Process Intensif. **121**, 24–49 (2017).
[19] H. Jiang, Y. Chen, S. Song, Z. Guo, Z. Zhang, C. Zheng, G. He, H. Wang, H. Wu, and T. Huang, Chem. Eng. J. **439**, 135657 (2022).
[20] M. Wang, P. Zhang, X. Liang, J. Zhao, Y. Liu, Y. Cao, H. Wang, Y. Chen, Z. Zhang, F. Pan, Z. Zhang, and Z. Jiang, Nat. Sustainability **5**(6), 518–526 (2022).
[21] Y. Wang, H. Jiang, Z. Guo, H. Ma, S. Wang, H. Wang, S. Song, J. Zhang, Y. Yin, H. Wu, Z. Jiang, and M. D. Guiver, Energy Environ. Sci. **16**(1), 53–75 (2023).
[22] H. Y. Chi, C. Chen, K. Zhao, L. F. Villalobos, P. A. Schouwink, L. Piveteau, K. P. Marshall, Q. Liu, Y. Han, and K. V. Agrawal, Angew. Chem. **134**(40), e202207457 (2022).
[23] L. F. Villalobos, M. T. Vahdat, M. Dakhchoune, Z. Nadizadeh, M. Mensi, E. Oveisi, D. Campi, N. Marzari, and K. V. Agrawal, Sci. Adv. **6**(4), eaay9851 (2020).
[24] Y. Wang, L. Li, Y. Wei, J. Xue, H. Chen, L. Ding, J. Caro, and H. Wang, Angew. Chem., Int. Ed. **56**(31), 8974–8980 (2017).
[25] Y. Wang, T. Lian, N. V. Tarakina, J. Yuan, and M. Antonietti, Nat. Commun. **13**(1), 7339 (2022).
[26] G. He, S. Huang, L. F. Villalobos, J. Zhao, M. Mensi, E. Oveisi, M. Rezaei, and K. V. Agrawal, Energy Environ. Sci. **12**(11), 3305–3312 (2019).
[27] S. Huang, M. Dakhchoune, W. Luo, E. Oveisi, G. He, M. Rezaei, J. Zhao, D. T. Alexander, A. Züttel, M. S. Strano, and K. V. Agrawal, Nat. Commun. **9**(1), 2632 (2018).
[28] S. Huang, S. Li, L. F. Villalobos, M. Dakhchoune, M. Micari, D. J. Babu, M. T. Vahdat, M. Mensi, E. Oveisi, and K. V. Agrawal, Sci. Adv. **7**(9), eabf0116 (2021).
[29] S. Wang, X. Li, H. Wu, Z. Tian, Q. Xin, G. He, D. Peng, S. Chen, Y. Yin, Z. Jiang, and M. D. Guiver, Energy Environ. Sci. **9**(6), 1863–1890 (2016).
[30] Y. Zhang, X. Feng, S. Yuan, J. Zhou, and B. Wang, Inorg. Chem. Front. **3**(7), 896–909 (2016).
[31] M. Galizia, W. S. Chi, Z. P. Smith, T. C. Merkel, R. W. Baker, and B. D. Freeman, Macromolecules **50**(20), 7809–7843 (2017).
[32] D. F. Sanders, Z. P. Smith, R. Guo, L. M. Robeson, J. E. McGrath, D. R. Paul, and B. D. Freeman, Polymer **54**(18), 4729–4761 (2013).
[33] M. Rezakazemi, M. Sadrzadeh, and T. Matsuura, Prog. Energy Combust. Sci. **66**, 1–41 (2018).
[34] W. F. Yong and H. Zhang, Prog. Mater. Sci. **116**, 100713 (2021).
[35] S. Kim and Y. M. Lee, Prog. Polym. Sci. **43**, 1–32 (2015).
[36] D. Li, Y. Yan, and H. Wang, Prog. Polym. Sci. **61**, 104–155 (2016).
[37] Y. Cheng, S. J. Datta, S. Zhou, J. Jia, O. Shekhah, and M. Eddaoudi, Chem. Soc. Rev. **51**(19), 8300–8350 (2022).
[38] Q. Qian, P. A. Asinger, M. J. Lee, G. Han, K. Mizrahi Rodriguez, S. Lin, F. M. Benedetti, A. X. Wu, W. S. Chi, and Z. P. Smith, Chem. Rev. **120**(16), 8161–8266 (2020).
[39] H. Dou, M. Xu, B. Wang, Z. Zhang, G. Wen, Y. Zheng, D. Luo, L. Zhao, A. Yu, L. Zhang, Z. Jiang, and Z. Chen, Chem. Soc. Rev. **50**(2), 986–1029 (2021).
[40] X. Li, Y. Liu, J. Wang, J. Gascon, J. Li, and B. Van der Bruggen, Chem. Soc. Rev. **46**(23), 7124–7144 (2017).
[41] L. Yang, S. Qian, X. Wang, X. Cui, B. Chen, and H. Xing, Chem. Soc. Rev. **49**(15), 5359–5406 (2020).
[42] C. Zhang, B. H. Wu, M. Q. Ma, Z. Wang, and Z. K. Xu, Chem. Soc. Rev. **48**(14), 3811–3841 (2019).
[43] M. Zhao, Y. Huang, Y. Peng, Z. Huang, Q. Ma, and H. Zhang, Chem. Soc. Rev. **47**(16), 6267–6295 (2018).
[44] J. H. Cavka, S. Jakobsen, U. Olsbye, N. Guillou, C. Lamberti, S. Bordiga, and K. P. Lillerud, J. Am. Chem. Soc. **130**(42), 13850–13851 (2008).

[45]G. Férey, C. Mellot-Draznieks, C. Serre, F. Millange, J. Dutour, S. Surblé, and I. Margiolaki, Science **309**(5743), 2040–2042 (2005).
[46]H. Furukawa, F. Gándara, Y.-B. Zhang, J. Jiang, W. L. Queen, M. R. Hudson, and O. M. Yaghi, J. Am. Chem. Soc. **136**(11), 4369–4381 (2014).
[47]S. Yuan, L. Feng, K. C. Wang, J. D. Pang, M. Bosch, C. Lollar, Y. J. Sun, J. S. Qin, X. Y. Yang, P. Zhang, Q. Wang, L. F. Zou, Y. M. Zhang, L. L. Zhang, Y. Fang, J. L. Li, and H. C. Zhou, Adv. Mater. **30**(37), 1704303 (2018).
[48]R. M. Far, B. Van der Bruggen, A. Verliefde, and E. Cornelissen, J. Chem. Technol. Biotechnol. **97**(3), 575–596 (2022).
[49]Y. Li and W. Yang, J. Membr. Sci. **316**(1–2), 3–17 (2008).
[50]N. Rangnekar, N. Mittal, B. Elyassi, J. Caro, and M. Tsapatsis, Chem. Soc. Rev. **44**(20), 7128–7154 (2015).
[51]X. Wang, Y. Zhang, X. Wang, E. Andres-Garcia, P. Du, L. Giordano, L. Wang, Z. Hong, X. Gu, S. Murad, and F. Kapteijn, Angew. Chem., Int. Ed. **58**(43), 15518–15525 (2019).
[52]J. Hou, Y. Wei, S. Zhou, Y. Wang, and H. Wang, Chem. Eng. Sci. **182**, 180–188 (2018).
[53]C. Yu, Y. Liang, W. Xue, Z. Zhang, X. Jia, H. Huang, Z. Qiao, D. Mei, and C. Zhong, J. Membr. Sci. **625**, 119139 (2021).
[54]Y. Li, L. Lin, M. Tu, P. Nian, A. J. Howarth, O. K. Farha, J. Qiu, and X. Zhang, Nano Res. **11**(4), 1850–1860 (2018).
[55]W. Li, P. Su, Z. Li, Z. Xu, F. Wang, H. Ou, J. Zhang, G. Zhang, and E. Zeng, Nat. Commun. **8**(1), 406 (2017).
[56]S. Zhou, O. Shekhah, A. Ramirez, P. Lyu, E. Abou-Hamad, J. Jia, J. Li, P. M. Bhatt, Z. Huang, H. Jiang, T. Jin, G. Maurin, J. Gascon, and M. Eddaoudi, Nature **606**(7915), 706–712 (2022).
[57]M. Jian, R. Qiu, Y. Xia, J. Lu, Y. Chen, Q. Gu, R. Liu, C. Hu, J. Qu, H. Wang, and X. Zhang, Sci. Adv. **6**(23), eaay3998 (2020).
[58]X. Ma, P. Kumar, N. Mittal, A. Khlyustova, P. Daoutidis, K. A. Mkhoyan, and M. Tsapatsis, Science **361**(6406), 1008–1011 (2018).
[59]Y. Peng, Y. Li, Y. Ban, H. Jin, W. Jiao, X. Liu, and W. Yang, Science **346**(6215), 1356–1359 (2014).
[60]S. Zhou, Y. Wei, L. Li, Y. Duan, Q. Hou, L. Zhang, L.-X. Ding, J. Xue, H. Wang, and J. Caro, Sci. Adv. **4**(10), eaau1393 (2018).
[61]F. Liu, Q. Li, J. Cui, Z. Li, G. Yang, Y. Liu, L. Dong, C. Xiong, H. Wang, and Q. Wang, Adv. Funct. Mater. **27**(20), 1606292 (2017).
[62]Y. Sun, J. Yan, Y. Gao, T. Ji, S. Chen, C. Wang, P. Lu, Y. Li, and Y. Liu, Angew. Chem. Int. Ed. **62**(15), e202216697 (2023).
[63]G. He, M. Dakhchoune, J. Zhao, S. Huang, and K. V. Agrawal, Adv. Funct. Mater. **28**(20), 1707427 (2018).
[64]R. Wei, H. Y. Chi, X. Li, D. Lu, Y. Wan, C. W. Yang, and Z. Lai, Adv. Funct. Mater. **30**(7), 1907089 (2019).
[65]Q. Hou, Y. Wu, S. Zhou, Y. Wei, J. Caro, and H. Wang, Angew. Chem., Int. Ed. **58**(1), 327–331 (2019).
[66]J. Luo, Y. Li, H. Zhang, A. Wang, W. S. Lo, Q. Dong, N. Wong, C. Povinelli, Y. Shao, S. Chereddy, S. Wunder, U. Mohanty, C. K. Tsung, and D. Wang, Angew. Chem., Int. Ed. **58**(43), 15313–15317 (2019).
[67]S. Zhou, O. Shekhah, T. Jin, J. Jia, S. J. Datta, P. M. Bhatt, and M. Eddaoudi, Chem **9**, 1182 (2023).
[68]P. Nian, H. Liu, and X. Zhang, J. Membr. Sci. **573**, 200–209 (2019).
[69]N. Wang, X. Li, L. Wang, L. Zhang, G. Zhang, and S. Ji, ACS Appl. Mater. Interfaces **8**(34), 21979–21983 (2016).
[70]Z. Qiao, Y. Liang, Z. Zhang, D. Mei, Z. Wang, M. D. Guiver, and C. Zhong, Adv. Mater. **32**(34), e2002165 (2020).
[71]W. Li, J. Shi, Z. Li, W. Wu, Y. Xia, Y. Yu, and G. Zhang, Adv. Mater. Interfaces **5**(14), 1800032 (2018).
[72]Y. Hu, J. Wei, Y. Liang, H. Zhang, X. Zhang, W. Shen, and H. Wang, Angew. Chem., Int. Ed. **55**(6), 2048–2052 (2016).
[73]H. T. Kwon and H. K. Jeong, J. Am. Chem. Soc. **135**(29), 10763–10768 (2013).
[74]V. Chernikova, O. Shekhah, and M. Eddaoudi, ACS Appl. Mater. Interfaces **8**(31), 20459–20464 (2016).
[75]H. Ang and L. Hong, ACS Appl. Mater. Interfaces **9**(33), 28079–28088 (2017).
[76]A. Pustovarenko, M. G. Goesten, S. Sachdeva, M. Shan, Z. Amghouz, Y. Belmabkhout, A. Dikhtiarenko, T. Rodenas, D. Keskin, I. K. Voets, B. M. Weckhuysen, M. Eddaoudi, L. de Smet, E. J. R. Sudholter, F. Kapteijn, B. Seoane, and J. Gascon, Adv. Mater. **30**(26), e1707234 (2018).
[77]Y. Peng and W. Yang, Adv. Mater. Interfaces **7**(1), 1901514 (2019).
[78]G. Liu, W. Jin, and N. Xu, Angew. Chem., Int. Ed. **55**(43), 13384–13397 (2016).
[79]M. J. Lee, H. T. Kwon, and H. K. Jeong, Angew. Chem., Int. Ed. **57**(1), 156–161 (2018).
[80]J. Hou, H. Zhang, G. P. Simon, and H. Wang, Adv. Mater. **32**(18), e1902009 (2020).
[81]B. Hosseini Monjezi, K. Kutonova, M. Tsotsalas, S. Henke, and A. Knebel, Angew. Chem., Int. Ed. **60**(28), 15153–15164 (2021).
[82]H. T. Kwon, H.-K. Jeong, A. S. Lee, H. S. An, and J. S. Lee, J. Am. Chem. Soc. **137**(38), 12304–12311 (2015).
[83]Y. Pan, T. Li, G. Lestari, and Z. Lai, J. Membr. Sci. **390–391**, 93–98 (2012).
[84]L. Shu, Y. Peng, R. Yao, H. Song, C. Zhu, and W. Yang, Angew. Chem., Int. Ed. **61**(14), e202117577 (2022).
[85]S. Zhou, O. Shekhah, J. Jia, J. Czaban-Jóźwiak, P. M. Bhatt, A. Ramírez, J. Gascon, and M. Eddaoudi, Nat. Energy **6**(9), 882–891 (2021).
[86]Y. Guo, Y. Ying, Y. Mao, X. Peng, and B. Chen, Angew. Chem., Int. Ed. **55**(48), 15120–15124 (2016).
[87]Y. Peng, Y. Li, Y. Ban, and W. Yang, Angew. Chem., Int. Ed. **56**(33), 9757–9761 (2017).
[88]Y. Zhu, J. Ciston, B. Zheng, X. Miao, C. Czarnik, Y. Pan, R. Sougrat, Z. Lai, C.-E. Hsiung, K. Yao, I. Pinnau, M. Pan, and Y. Han, Nat. Mater. **16**(5), 532–536 (2017).
[89]X. Wang, Q. Lyu, T. Tong, K. Sun, L. C. Lin, C. Y. Tang, F. Yang, M. D. Guiver, X. Quan, and Y. Dong, Nat. Commun. **13**(1), 266 (2022).
[90]Y. Liu, Z. Ng, E. A. Khan, H.-K. Jeong, C.-b. Ching, and Z. Lai, Microporous Mesoporous Mater. **118**(1–3), 296–301 (2009).
[91]H. Bux, F. Liang, Y. Li, J. Cravillon, M. Wiebcke, and J. Caro, J. Am. Chem. Soc. **131**(44), 16000–16001 (2009).
[92]X. Liu, W. Fu, and E. Bouwman, Chem. Commun. **52**(42), 6926–6929 (2016).
[93]S. Fan, F. Sun, J. Xie, J. Guo, L. Zhang, C. Wang, Q. Pan, and G. Zhu, J. Mater. Chem. A **1**(37), 11438–11442 (2013).
[94]V. I. Isaeva, M. I. Barkova, L. M. Kustov, D. A. Syrtsova, E. A. Efimova, and V. V. Teplyakov, J. Mater. Chem. A **3**(14), 7469–7476 (2015).
[95]X. Wu, C. Liu, J. Caro, and A. Huang, J. Membr. Sci. **559**, 1–7 (2018).
[96]R. Ranjan and M. Tsapatsis, Chem. Mater. **21**(20), 4920–4924 (2009).
[97]J. Hao, D. J. Babu, Q. Liu, H.-Y. Chi, C. Lu, Y. Liu, and K. V. Agrawal, J. Mater. Chem. A **8**(16), 7633–7640 (2020).
[98]I. Stassen, M. Styles, G. Grenci, H. V. Gorp, W. Vanderlinden, S. D. Feyter, P. Falcaro, D. D. Vos, P. Vereecken, and R. Ameloot, Nat. Mater. **15**(3), 304–310 (2016).
[99]M. Q. Seah, W. J. Lau, P. S. Goh, H.-H. Tseng, R. A. Wahab, and A. F. Ismail, Polymers **12**(12), 2817 (2020).
[100]Y. Xiao, W. Zhang, Y. Jiao, Y. Xu, and H. Lin, J. Membr. Sci. **624**, 119101 (2021).
[101]E. Shamsaei, X. Lin, L. Wan, Y. Tong, and H. Wang, Chem. Commun. **52**(95), 13764–13767 (2016).
[102]S. Hurrle, S. Friebe, J. Wohlgemuth, C. Woll, J. Caro, and L. Heinke, Chem. Eur. J. **23**(10), 2294–2298 (2017).
[103]X. Wang, C. Chi, K. Zhang, Y. Qian, K. M. Gupta, Z. Kang, J. Jiang, and D. Zhao, Nat. Commun. **8**, 14460 (2017).
[104]H. Song, Y. Peng, C. Wang, L. Shu, C. Zhu, Y. Wang, H. He, and W. Yang, Angew. Chem. Int. Ed. **62**(17), e202218472 (2023).
[105]X. Duan, P. Kaya, H.-Y. Chi, B. Topuz, and K. V. Agrawal, J. Membr. Sci. Lett. **3**(1), 100045 (2023).
[106]X. Ma, Z. Wan, Y. Li, X. He, J. Caro, and A. Huang, Angew. Chem., Int. Ed. **59**(47), 20858–20862 (2020).
[107]A. Knebel, L. Sundermann, A. Mohmeyer, I. Strauß, S. Friebe, P. Behrens, and J. Caro, Chem. Mater. **29**(7), 3111–3117 (2017).
[108]J. Wang, Y. Wang, Y. Liu, H. Wu, M. Zhao, Y. Ren, Y. Pu, W. Li, S. Wang, and S. Song, Adv. Funct. Mater. **32**, 2208064 (2022).
[109]D. S. Sholl and R. P. Lively, Nature **532**(7600), 435 (2016).

[110]E. S. Rubin, J. E. Davison, and H. J. Herzog, Int. J. Greenhouse Gas Control **40**, 378–400 (2015).
[111]E. Favre, J. Membr. Sci. **294**(1–2), 50–59 (2007).
[112]L. Peters, A. Hussain, M. Follmann, T. Melin, and M. B. Hägg, Chem. Eng. J. **172**(2–3), 952–960 (2011).
[113]D. J. Babu, G. He, J. Hao, M. T. Vahdat, P. A. Schouwink, M. Mensi, and K. V. Agrawal, Adv. Mater. **31**(28), e1900855 (2019).
[114]Y. Ren, X. Liang, H. Dou, C. Ye, Z. Guo, J. Wang, Y. Pan, H. Wu, M. D. Guiver, and Z. Jiang, Adv. Sci. **7**(19), 2001398 (2020).
[115]A. Deng, X. Shen, Z. Wan, Y. Li, S. Pang, X. He, J. Caro, and A. Huang, Angew. Chem. **133**(48), 25667–25671 (2021).
[116]Y. Song, Y. Sun, D. Du, M. Zhang, Y. Liu, L. Liu, T. Ji, and G. He, J. Membr. Sci. **634**, 119393 (2021).
[117]S. Chen, Y. Liu, Y. Sun, G. Xu, T. Ji, X. Zhang, and F. Wang, J. Membr. Sci. **643**, 120064 (2022).
[118]F. K. Kessler, Y. Zheng, D. Schwarz, C. Merschjann, W. Schnick, X. C. Wang, and M. J. Bojdys, Nat. Rev. Mater. **2**(6), 17030 (2017).
[119]Z. Lai, Curr. Opin. Chem. Eng. **20**, 78–85 (2018).
[120]Q. Ma, K. Mo, S. Gao, Y. Xie, J. Wang, H. Jin, A. Feldhoff, S. Xu, J. Y. S. Lin, and Y. Li, Angew. Chem., Int. Ed. **59**(49), 21909–21914 (2020).
[121]C. J. T. Grotthuss, "Sur la décomposition de l'eau et des corps qu'elle tient en dissolution à l'aide de l'électricité galvanique," Ann. Chim. **58**, 54–74 (1806).
[122]K.-D. Kreuer, A. Rabenau, and W. Weppner, Angew. Chem. Int. Ed. **21**(3), 208–209 (1982).
[123]T. Ueki and M. Watanabe, Macromolecules **41**(11), 3739–3749 (2008).
[124]R. Epsztein, R. M. DuChanois, C. L. Ritt, A. Noy, and M. Elimelech, Nat. Nanotechnol. **15**(6), 426–436 (2020).
[125]F. Yang, G. Xu, Y. Dou, B. Wang, H. Zhang, H. Wu, W. Zhou, J. R. Li, and B. Chen, Nat. Energy **2**(11), 877 (2017).
[126]Q. Y. Liu, Z. K. Li, D. H. Wang, Z. F. Li, X. L. Peng, C. B. Liu, and P. L. Zheng, Front. Chem. **8**, 694 (2020).
[127]R. Annapragada, K. R. Vandavasi, and P. R. Kanuparthy, Inorg. Chim. Acta **546**, 121304 (2023).
[128]W. J. Phang, H. Jo, W. R. Lee, J. H. Song, K. Yoo, B. Kim, and C. S. Hong, Angew. Chem. **127**(17), 5231–5235 (2015).
[129]M. Sadakiyo, T. Yamada, and H. Kitagawa, J. Am. Chem. Soc. **131**(29), 9906–9907 (2009).
[130]F.-M. Zhang, L.-Z. Dong, J.-S. Qin, W. Guan, J. Liu, S.-L. Li, M. Lu, Y.-Q. Lan, Z.-M. Su, and H.-C. Zhou, J. Am. Chem. Soc. **139**(17), 6183–6189 (2017).
[131]Y. Guo, Z. Jiang, W. Ying, L. Chen, Y. Liu, X. Wang, Z. J. Jiang, B. Chen, and X. Peng, Adv. Mater. **30**(2), 1705155 (2018).
[132]H. Q. Liang, Y. Guo, Y. Shi, X. Peng, B. Liang, and B. L. Chen, Angew. Chem., Int. Ed. **59**(20), 7732–7737 (2020).
[133]X. Y. Li, H. C. Zhang, H. Yu, J. Xia, Y. B. Zhu, H. A. Wu, J. Hou, J. Lu, R. W. Ou, C. D. Easton, C. Selomulya, M. R. Hill, L. Jiang, and H. T. Wang, Adv. Mater. **32**(24), 2001777 (2020).
[134]X. Li, M. R. Hill, H. Wang, and H. Zhang, Adv. Mater. Technol. **6**(10), 2000790 (2021).
[135]D. Shi, X. Yu, W. Fan, V. Wee, and D. Zhao, Coord. Chem. Rev. **437**, 213794 (2021).
[136]H. Zhang, X. Li, J. Hou, L. Jiang, and H. Wang, Chem. Soc. Rev. **51**(6), 2224–2254 (2022).
[137]H. Zhang, J. Hou, Y. Hu, P. Wang, R. Ou, L. Jiang, J. Z. Liu, B. D. Freeman, A. J. Hill, and H. Wang, Sci. Adv. **4**(2), eaaq0066 (2018).
[138]J. Lu, H. Zhang, J. Hou, X. Li, X. Hu, Y. Hu, C. D. Easton, Q. Li, C. Sun, A. W. Thornton, M. R. Hill, X. Zhang, G. Jiang, J. Z. Liu, A. J. Hill, B. D. Freeman, L. Jiang, and H. Wang, Nat. Mater. **19**(7), 767–774 (2020).
[139]T. Xu, M. A. Shehzad, D. Yu, Q. Li, B. Wu, X. Ren, L. Ge, and T. Xu, Chemsuschem **12**(12), 2593–2597 (2019).
[140]T. Xu, M. A. Shehzad, X. Wang, B. Wu, L. Ge, and T. Xu, Nano-Micro Lett. **12**(1), 51 (2020).
[141]H. Q. Liang, Y. Guo, X. Peng, and B. Chen, J. Mater. Chem. A **8**(22), 11399–11405 (2020).
[142]J. Wang, R. Fang, J. Hou, H. Zhang, Y. Tian, H. Wang, and L. Jiang, ACS Nano **11**(3), 3022–3029 (2017).
[143]X. Li, H. Zhang, J. Hou, R. Ou, Y. Zhu, C. Zhao, T. Qian, C. D. Easton, C. Selomulya, M. R. Hill, and H. Wang, J. Am. Chem. Soc. **142**(21), 9827–9833 (2020).
[144]J. Lu, G. Jiang, H. Zhang, B. Qian, H. Zhu, Q. Gu, Y. Yan, J. Z. Liu, B. D. Freeman, L. Jiang, and H. Wang, Sci. Adv. **9**(4), eabq1369 (2023).
[145]J. Lu, H. Zhang, X. Hu, B. Qian, J. Hou, L. Han, Y. Zhu, C. Sun, L. Jiang, and H. Wang, ACS Nano **15**(1), 1240–1249 (2021).
[146]J. Hou, H. C. Zhang, J. Lu, X. Y. Li, C. Zhao, H. T. Wang, A. W. Thornton, and K. Konstas, J. Membr. Sci. **674**, 121511 (2023).
[147]X. Li, H. Zhang, P. Wang, J. Hou, J. Lu, C. D. Easton, X. Zhang, M. R. Hill, A. W. Thornton, J. Z. Liu, B. D. Freeman, A. J. Hill, L. Jiang, and H. Wang, Nat. Commun. **10**, 2490 (2019).
[148]P. Ramirez, P. Y. Apel, J. Cervera, and S. Mafé, Nanotechnology **19**(31), 315707 (2008).
[149]D. L. Zhao, F. Feng, L. G. Shen, Z. Y. Huang, Q. P. Zhao, H. J. Lin, and T. S. Chung, Chem. Eng. J. **454**, 140447 (2023).
[150]N. Abdullah, N. Yusof, A. F. Ismail, and W. J. Lau, Desalination **500**, 114867 (2021).
[151].1039/c6cs00362aC. Wang, X. Liu, N. Keser Demir, J. P. Chen, and K. Li, Chem. Soc. Rev. **45**(18), 5107–5134 (2016).
[152]Y. C. Xu, Y. R. Xiao, W. T. Zhang, H. J. Lin, L. G. Shen, R. J. Li, Y. Jiao, and B. Q. Liao, J. Membr. Sci. **618**, 118726 (2021).
[153]H. Zhang, D. Liu, Y. Yao, B. Zhang, and Y. S. Lin, J. Membr. Sci. **485**, 103–111 (2015).
[154]H. Wang, M. Jian, Z. Qi, Y. Li, R. Liu, J. Qu, and X. Zhang, Microporous Mesoporous Mater. **259**, 171–177 (2018).
[155]H. Zhang, M. Zhao, and Y. S. Lin, Microporous Mesoporous Mater. **279**, 201–210 (2019).
[156]Q. Liu, Y. Miao, L. F. Villalobos, *et al.*, "Unit-cell-thick zeolitic imidazolate framework films for membrane application," Nature Materials (in press) (2023).
[157]Y. Pan, B. Wang, and Z. Lai, J. Membr. Sci. **421–422**, 292–298 (2012).